POLITECNICO DI TORINO

Corso di Laurea
in Ingegneria Aerospaziale

Tesi di Laurea Magistrale

Development and integration of a FBG optical sensor network for prognostics of electromechanical actuators.

Relatori
Prof. Matteo D.L. Dalla Vedova
Prof. Paolo Maggiore
Ing. Alessandro Aimasso
Ing. Pier Carlo Berri

Candidato
Francesco Gerbino

firma dei relatori

....
....

firma del candidato

....

Anno Accademico 2021-2022

Abstract

This thesis was developed at the Mechanical and Aerospace Engineering Department (DIMEAS) of the Politecnico di Torino.

With the strong development of the more-eletric philosophy for aircraft, EMAs (Electro-mechanical actuators) are increasingly being used and represent a critical safety element. The development of prognostic algorithms makes it possible to increase the safety levels of EMAs. In this scenario a key role is played by sensors that enable the acquisition of input data for prognostic algorithms. FBGs (Fiber bragg gratings) are innovative sensors that are very adaptable to the aerospace environment. FBGs guarantee high performances in terms of accuracy and sensibilty and offer a number of advantages over traditional sensors: they are immune to the electromagnetic interferences, they are light and small, and can be installed in series on the same cable. The objective of this work is the development and integration of a FBG optical sensors network for prognostics on the Gearbox of an experimental test bench reproducing an electromechanical servomechanism. The first step, before the installation of FBGs, was the design of a Load-module that can simulate an external load on the Gearbox, so that the FBGs can be used to evaluate the structural deformations caused by the load. Later, FBGs were installed together with strain gauges on the surface of the Gearbox made from PLA, which was connected to the motor shaft. The curved installation surface and the material of the Gearbox led to the development of a specific procedure for installing the sensors. Tests were carried out in order to evaluate the deformations measured by FBGs and strain gauges, when an external load is applied on the Gearbox through the Load module. Finally, the comparison of the data from the two types of sensors made it possible to calibrate and evaluate the FBGs as prognostic sensors for the electromechanical actuators.

Contents

List of Tables

List of Figures

Chapter 1

Introduction

In recent decades, enormous progress has been made in the transition to more electric aircraft. The approach of the more electric philosophy is to replace pneumatic, mechanical and hydraulic sources of power generation with electric power, in order to have a single, more manageable power source. This implies that many subsystems typically powered by pneumatic and hydraulic power begin to be replaced with subsystems powered by electric power.

In particular, all primary controls are typically driven by hydraulic servomechanisms. This is because in addition to their power, hydraulic actuators lend themselves very well to continuous operation, as is the case with primary controls, and above all they are very reliable. However, hydraulic actuators require a dedicated hydraulic system, which transports the power from the motors to the actuators located on the various control surfaces.

The hydraulic system is heavy, complex and requires constant and expensive maintenance. Therefore, the use of electromechanical actuators, powered by electricity, is the idea that has developed in recent years. This would guarantee the complete elimination of the hydraulic system. Currently, EMAs are used in the most modern aircraft to actuate the secondary flight controls[4].

The idea is to introduce them for the primary flight controls as well, but for this to happen it is necessary for EMAs to reach very high safety levels, comparable to hydraulics. Prognostic algorithms can be a way of monitoring the behaviour of EMA actuators and thus can increase the safety level of these subsystems.

Prognostic algorithms can be used to estimate whether there are fault conditions, such as local overheating or component degradation, and thus can be useful both for scheduling maintenance and for making EMAs safer.

In order to function, prognostic algorithms require a set of data on the operating parameters of the servomechanism; the effectiveness of the algorithm is closely linked to the performance of the sensors that are able to collect this data, which serve as input for the prognostic algorithm. So the sensors used is a very critical aspect of the prognostic cycle.

FBGs (fiber bragg gratings) are fiber-optic sensors that provide high levels of performance and are very well suited to the aerospace environment. Specifically, FBGs are immune to electromagnetic interference, they are lightweight and resist temperature well. When installed on specific parts of electromechanical servomechanisms, FBGs can provide important information regarding structural deformations, component stresses or about local temperature variations. Structural deformations can be traced back to loads discharging on the servomechanism, while local temperature rises in the vicinity of the electric motor may indicate excessive power dissipation and thus electrical faults.

The aim of this thesis is to install a network of FBG sensors on a test bench and to investigate how they can be useful for measuring structural deformations when the servomechanism is subjected to a variable external load. In order to simulate a load on the servomechanism, a load-module was designed, which simulates an external load on the test bench gearbox (e.g. aerodynamic load). During a series of experimental tests, the behaviour of FBGs will be compared with that of strain gauges, which represent a known and reliable technology. However, FBGs could offer a number of advantages over strain gauges, as they are lighter, can be installed in series on the same optical cable and are not subject to electromagnetic interference. The structure of the document is shown next.

- **Chapter 1: Introduction** The concepts of more-electric, electromechanical actuators and prognostic algorithms are explained in this introductory chapter.
- **Chapter 2: Optical Fibers** This chapter explains the theory of fiber optics, the FBGs working principles and their main aspects.
- **Chapter 3: Test bench** This chapter describes the architecture of the test bench on which the fibers and load module were installed. All the devices present and their interactions are explained, as well as the general operation of the test bench.
- **Chapter 4: Design of the Load Module** This chapter is about the load-module, through which an external load is simulated on the servomechanism. The chapter explains the design of the load module, its architecture, operation and validation.
- **Chapter 5: Installation of FBG sensors and strain gauges** The unconventional geometry of the installation surface required the development of a specific procedure, this chapter explains the installation procedure used for FBGs and strain gauges.
- **Chapter 6: Experimental tests and Results** This chapter sets out the procedure used to carry out the tests. Then, the results obtained on the validation of FBGs are presented and commented.

1.1 More electric

In recent years, the aviation industry has focused on increasing the efficiency of aircraft so that energy consumption and related costs can be reduced.

In a conventional aircraft, there are many different subsystems that need to be powered by different types of power, so there is mechanical power, hydraulic power, electrical power, and pneumatic power. All these types of power are in most cases derived from the power generated by the engines. For example, mechanical power is extracted directly from a driven shaft and then, thanks to gearboxes, it is used to drive fuel pumps, hydraulic pumps and electric generators, in this way, mechanical power is converted into hydraulic power and electrical power. Pneumatic power, on the other hand, is extracted directly from the compressor and then used to power the Enviromental control system (ECS).

From an efficiency point of view, the presence of all these power systems is not advantageous: the continuous conversion of power from one form to another is limited by efficiencies that overall result in a considerable expenditure of energy. Another problem is that all power distribution systems must be present on the aircraft: hydraulic hoses, pneumatic hoses, mechanical transmissions, electrical cables. This causes a general increase in weight, aircraft complexity, and maintenance costs.

For all these reasons, the modern aviation industry is moving towards a new design philosophy, called more-electric. The idea of the more electric is to use electricity as the only source of power, in this way, all other power sources and transport systems can be removed with advantages in terms of weight, cost and complexity. To do this, subsystems must be capable of being powered by electricity, so the entire system architecture in more-electric aircraft must be rethought and differs greatly from that of conventional aircraft. A comparison between a traditional and a more electric architecture is shown in the next figure.

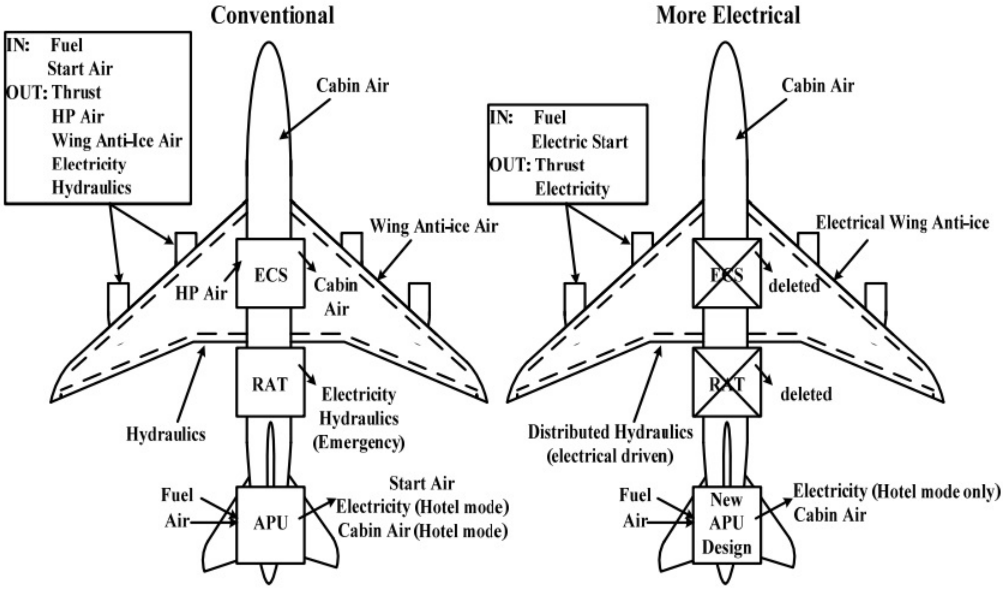

Figure 1.1. Comparison between conventional and more-electric aircraft

Some of the benefits of more electric architecture are[3]:

- The removal of the hydraulic system reduces installation and operating costs, weight, complexity, redundancy.
- Electrical starting of the engine through the engine starter/generator eliminates the engine tower shaft and gears, power take-off shaft, accessory gearboxes, and reduces power needed to start the engine, especially in the cold scenarios.
- it's possible to replace the engine-bleed system with electric motor-driven pumps, reducing costs and complexity.

In conclusion, the more electric design philosophy offers many advantages but requires the development and integration of electrically powered subsystems, such as EMAs (Electro-mechanical actuators).

1.2 EMA

EMAs (Electro-mechanical actuators) are currently typically used to operate secondary flight controls: on Boeing 787 they are used for landing gear braking, mid spoiler surfaces, and trimmable horizontal stabilizer, on A380 EMA are used for slats, horizontal stabilizer, and thrust reverser actuation[4].

There are two types of EMA:

1. **Linear EMA:**The rotation of the electric motor is transformed into linear movement of the actuator by means of a screw mechanism. In linear EMAs, there can be a gearbox between the motor and the actuator and they are called geared EMAs or they can be direct drive, in which case they are called direct drive EMAs.

2. **Rotary EMA:**The output of these actuators is a rotary motion. A gearbox is interposed between the electric motor and the actuator, which allows the torque and angular speed to be changed via a reduction ratio.

In the test bench used for this thesis project, a rotary EMA is installed, its characteristics will be explained later in Chapter 3.

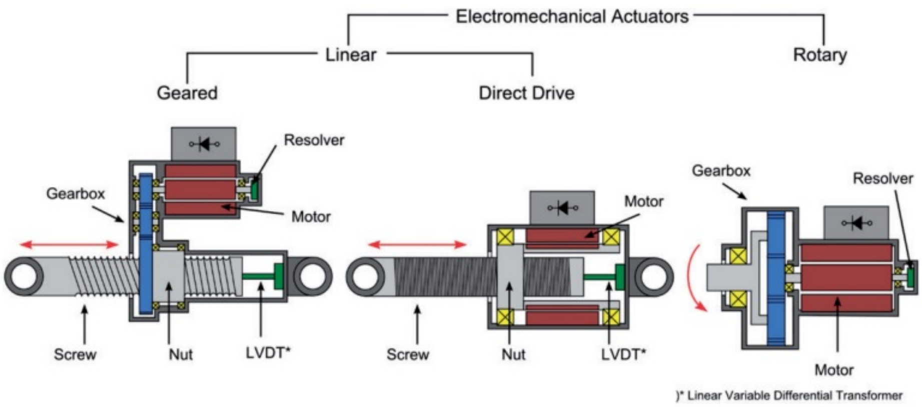

Figure 1.2. Classification of different EMA types

1.3 Prognostics and Health Management (PHM)

Prognostics and Health Management (PHM) is the science that studies the health state of a system and predicts its evolution in the future. This concept is very applicable to control systems and actuators such as EMAs, because it allows much more efficient maintenance strategies to be implemented and actuators to be constantly monitored, increasing their level of safety and reliability.

A PHM algorithm can be implemented considering two different approaches:

- **Model-based PHM:** models are created that represent in detail the physical phenomena affecting the health state. In this case a very thorough knowledge of the physical phenomena and degradation mechanisms of the system is required to create realistic models.
- **Data-driven PHM:** some system data are monitored before it fails, so that it is possible to reconstruct the system's behaviour before failure and use this knowledge to predict failures. In this case, it is not necessary to know the physical models of degradation and failure in a strict detail.

Recently, the new PHM algorithms are conceived in a hybrid form, so they use monitoring data to reconstruct system behaviour but also use some physical models of the system. A PHM algorithm must perform three main tasks:

1. **Fault detection:** the algorithm must be able to distinguish abnormal behaviours from all normal behaviours and isolate them, otherwise the fault cannot be identified.
2. **Fault diagnosis:** there are different classifications for faults, so the algorithm must be able to identify the type of fault and distinguish it from all others that can be verified.
3. **Degradation prediction:** finally, the algorithm must be able to predict the effects of the malfunction in order to estimate the RUL (Remaining Useful Life).

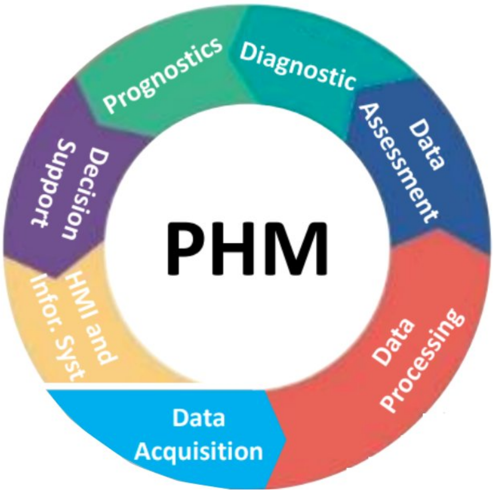

Figure 1.3. PHM Cycle

The operating cycle of a PHM algorithm is shown in the Figure 1.3. Initially, using the sensors installed on the physical component, it is possible to collect and save input data for the algorithm. At this stage, it is very important that the data are reliable and therefore the sensors ensure adequate performances. Furthermore, it is essential to establish what kind of data should be taken and in what modality. This phase is called *Data Acquisition*. Then follows *Data processing*: data are cleaned of measurement noise and analyses are performed on the data, either in the time domain or in the frequency domain, evaluating both their trend and magnitude. Then in the *Data assessment*, it is checked whether the collected data are in line with the expected behaviour of the system or whether there are inconsistencies due to anomalies, for example. In the *Diagnostic phase*, the fault is identified and classified and possible consequences are estimated. The *prognostic phase* assesses the RUL of the system and the effects of the failure on its health. Finally, in the final decision phase, the maintenance intervention to be carried out is chosen, based on the type of fault. Thus, prognostic sensors are a critical element in the acquisition of input data for the PHM algorithm, as their characteristics and installation can strongly influence the effectiveness of the algorithm. In the next chapter, the functioning of Optical fibers and FBGs are introduced.

Chapter 2

Optical Fibers

In recent years, there has been a strong development of prognostic algorithms applied to electromechanical actuators, with the aim of increasing the safety and reliability of these devices. The accuracy of prognostic algorithms is closely linked to the sensors that are used to acquire the data.

FBGs are very interesting when used as prognostic sensors on EMAs, as they can provide a number of useful input parameters and they can replace other sensors such as strain gauges, offering some advantages that will be discussed next.

In that sense, FBGs (Fiber Bragg gratings) are very applicable to the aerospace context, because they provide reliability, sensibility, and are not subject to electromagnetic disturbances. The FBGs allow measurement of structural deformations and temperature changes; these two quantities can provide important information on the presence of anomalies such as excessive mechanical stresses in the servomechanism, the presence of local overheating due to stator windings short-circuit, power electronic failure or excessive dissipation due to friction[7].

This thesis project is focused on evaluating the use of FBGs on the outer structure of the gearbox as sensors to assess structural deformation. FBGs were installed on some strategic points on the gearbox, which are more prone to mechanical deformations, and tests were conducted to evaluate the behavior of the fibers when an external load is simulated on the servomechanism. This chapter will introduce the characteristics and working principle of Optical fibers.

2.1 Introduction to optical fibers

Optical fibers are filaments of glassy or polymeric materials that allow high-frequency electromagnetic waves to be transported within them, with extremely limited losses. Fiber is normally made of pure silica due to its pure qualities and the properties that give it good total internal refraction.

Fiber is formed by three layers:

- **Core**
- **Cladding**
- **Coating**

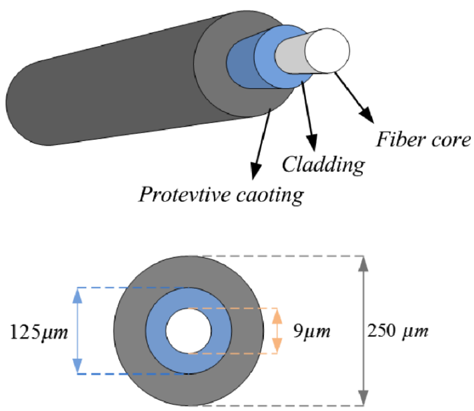

Figure 2.1. Fiber Layers

The fiber works in the same way as a cylindrical mirror: light is transmitted inside of the cable due to a series of light reflections on the separating surface between the innermost state (the core) and the state that surrounds it (the cladding). The cladding always has a lower refractive index than the core, and a thickness greater than the damping length of the evanescent wave. In this way, even the small percentage of light that is not reflected in the core is captured by the cladding. Types of fibers differ in layer thickness and materials used. In Figure 2.1 there is a schematic view of a single-mode fiber, which has a core diameter of 9um, much smaller than the cladder, which has a diameter of 125 um. However, there are other types of fibers called Multimodes that have a much thicker core that can be as thick as 62.5 um.

2.1.1 Types of optical fibers

The way light propagates within the core depends on the type of fiber, there are mainly three types of fiber and three related propagation modes.

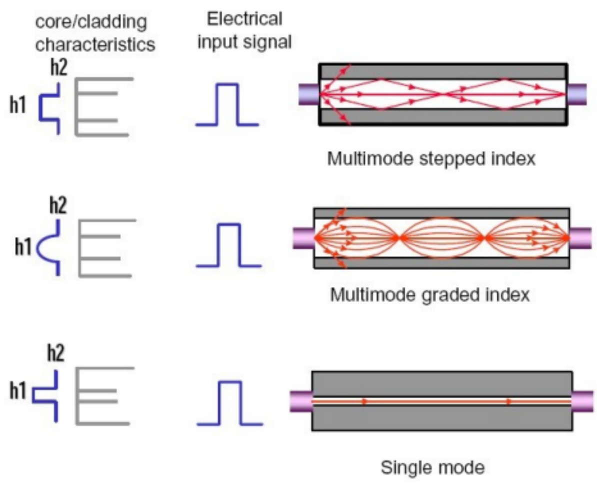

Figure 2.2. Fiber Types

- **Step-Index Multimode Fiber:** This type of fiber is characterized by a very large diameter. The name step-index is given by refractive index discontinuity between the core and the cladding.This type of fiber can have many propagation modes. Because of modal dispersion, the signal loses some of its shape and thus data rates are lower.

- **Gradient-Index Multimode Fiber:** That type of fiber is the most widely used today. In this fiber, the core has a variable refractive index with a parabolic pattern, which decreases moving from the center of the core toward the cladder. In this way, modal dispersion is reduced.
- **Single-mode optical Fiber:** In this type of fiber the core diameter is so small that light flows through it without reflections, so losses are minimized because there are no modal dispersions. This type of fiber is used for long distances, but can only be used with a laser source.

2.1.2 Fiber optic theory

The working principle of optical fibers as a signal transmission system is based on the physical principle summarized by Snell's law.

$$n_1 sin(\theta_1) = n_2 sin(\theta_2) \tag{2.1}$$

In (2.1):

- n_1 and n_2 are the refractive indexes of the materials.
- θ_1 is the angle of incidence formed between the ray of light and the normal to the surface on which it reflects.
- θ_2 is the angle formed between the refracted ray and the normal to the surface.

By Snell's law, it is possible to define a critical angle of incidence θ_c beyond which total ray reflection occurs.

$$\theta_c = \arcsin \frac{n_2}{n_1} \tag{2.2}$$

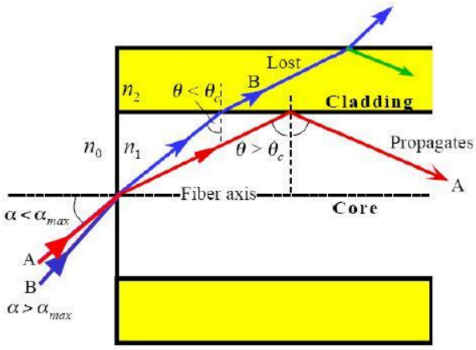

Figure 2.3. Angle of a fiber optic

When the angle of incidence between ray and surface normal is greater than the critical angle then total reflection occurs and there is no dissipation loss. Conversely, if the angle of incidence with respect to the normal is small, part of the signal will be absorbed by the cladder and will not be reflected within the core. For obvious reasons then in optical fibers the angle of incidence is such that there is always total reflection. A much more useful angle to evaluate to understand the fiber's reflection limits is the angle α_{max}. For geometric considerations from the graph 2.3 it can be written:

$$n_0 sin(\alpha) = n_1 sin(\frac{\pi}{2} - \theta_c) \tag{2.3}$$

From here it can be derived that:

$$sin(\alpha_{max}) = \frac{(n_1^2 - n_2^2)^{1/2}}{n_0} \tag{2.4}$$

In the above equation n_0 is refractive index of the external medium, which is generally air. The numerical aperture NA is defined:

$$NA = (n_1^2 - n_2^2)^{1/2} \tag{2.5}$$

It is finally derived:

$$\alpha_{max} = \arcsin \frac{NA}{n_0} \tag{2.6}$$

2.1.3 Advantages and disadvantages of optical fibers

Optical Fibers are very competitive products in telecommunications and also in aerospace. The main advantages of fiber optics over other more traditional techonlogies, such as copper cables, are:

- Fiber optics are not vulnerable to electromagnetic interference. In aerospace application this is a great advantage, in fact electronic devices often work simultaneously and close together, so they are subject to electromagnetic interference which is a widespread problem and safety risk.
- They have very low signal attenuations and thus allow data to be transferred over long distances at high speeds and without losing data quality during transmission.
- They are safe for aerospace applications because they do not overheat and do not produce sparks that can potentially cause fires.
- They do not conduct electricity because they are made of glass and dielectric coating materials.
- Fiber optics are resistant to extreme environments, as they withstand high temperatures and corrosive environments well. Unlike cables made of metallic material that are prone to corrosion and high temperatures.
- Fiber optics are lighter than copper links.
- They are made of glass, which is a more readily available and inexpensive material than copper.

Fiber optics also have disadvantages that are essential to evaluate when considering their application in an industrial setting. Specifically:

- The fibers are delicate and therefore must be protected to withstand mechanical stresses without breaking.
- Fiber optics are more complicated to install and cannot be bent beyond a certain radius of curvature, as they would be subject to excessive signal loss.

- When used as sensors, as in the case of FBGs, they play a passive role and thus require a relatively complex and expensive interrogation system to acquire sensor data.

- Fiber maintenance is a complicated and expensive process.

2.2 Fiber Bragg grating sensors (FBG)

Optical Fiber are many used in telecommunications, to transmit large amounts of data over long distances. However, recently optical fibers are also being used as passive sensors, to evaluate quantities such as strain or temperature changes. FBG (Fiber Bragg grating) sensors are an example of this specific application.

A Fiber Bragg grating (FBG) is a type of distributed Bragg reflector constructed in a short segment of optical fiber, typically about 1cm. In the innermost part of the core, refractive index changes are introduced, through a Bragg grating. In this way when a signal arrives in the vicinity of the grating the fiber will be able to reflect certain wavelengths and transmit others. The operation of the FBG as a sensor is based on this principle. The Bragg grating pitch Λ_b is fixed and thus the Bragg reflected wavelength λ_b can be calculated as:

$$\lambda_b = 2n_{eff}\Lambda_b \tag{2.7}$$

- λ_b is the Bragg reflected wavelength.

- n_{eff} is the refractive index of the core.

- Λ_b is the Bragg grating pitch.

When there is a change in the distance between photoengravings within the Bragg, a change in the reflected wavelength is observed, so Λ_b changes. Deformation of the Bragg can occur due to an external mechanical strain that compresses or tensions the FBG relative to its rest condition. Temperature variation is another factor that can affect the grating pitch and thus the reflected wavelength.

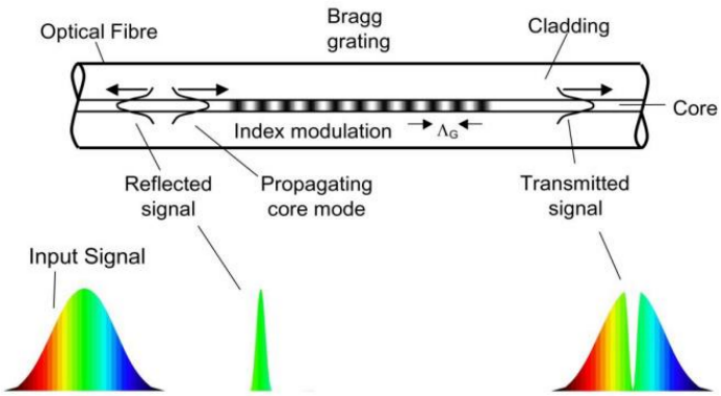

Figure 2.4. FBG working principle

2.2.1 Mechanical deformation

If the Bragg wavelength is derived, we obtain:

$$\frac{\Delta\lambda_b}{\lambda_b} = \frac{\Delta(n_{eff}\Lambda)}{n_{eff}\Lambda} = (1 + \frac{1}{n_{eff}\partial}\frac{\partial n_{eff}}{\partial\epsilon})\Delta\epsilon = (1 + p_e)\Delta\epsilon = \beta_\epsilon\Delta\epsilon \tag{2.8}$$

In the previous equation:

- $\Delta\epsilon$ is the mechanical deformation.
- $\frac{\Delta\lambda_b}{\lambda_b}$ is the relative change in reflected wavelength from the initial wavelength reflected at rest.
- p_e is the photoelastic constant (≈-0.212)
- β_ϵ is the sensitivity to deformation of the grid (≈-0.788).

The reflected wavelength varies proportionally to the mechanical strain applied to the FBG, due to the factor β_ϵ.

2.2.2 Thermal deformation

The reflected wavelength can also change due to a temperature change near the Bragg. Specifically, it can be derived:

$$\frac{\Delta\lambda_b}{\lambda_b} = \frac{\Delta(n_{eff}\Lambda)}{n_{eff}\Lambda} = (\frac{1}{\Lambda}\frac{\Lambda}{\partial T} + \frac{1}{n_{eff}}\frac{\partial n_{eff}}{\partial T})\Delta T = (\alpha + \zeta)\Delta T = \beta_T \Delta T \tag{2.9}$$

- β_T is the sensitivity to thermal of the grid.
- α coefficient of thermal expansion of fiber.
- ζ thermo-optical coefficient.

When the FBG is subjected to a temperature change ΔT, a proportional wavelength change is generated, which depends on a factor β_T.

2.2.3 Total deformation

$$\frac{\Delta\lambda_b}{\lambda_b} = (1 + p_e)\Delta\epsilon + (\alpha + \zeta)\Delta T = \beta_\epsilon \Delta\epsilon + \beta_T \Delta T \tag{2.10}$$

In a real application context any change in the wavelength of the FBG may be due to the simultaneous action of a mechanical strain and a thermal strain. The effects can be considered simultaneously, and it's possible to calculate the relative Bragg wavelength change, as is shown in Equation 2.10.

Chapter 3

Test bench architecture

3.1 Genereal overview

The test bench reproduces all parts of an electromechanical servomechanism. This makes it possible to have a detailed real model, from which to obtain actual data on the functioning of the servomechanism. Real data can be compared for example with the data obtained through the simulation of a Simulink model, which reproduces the test bench in all its parts. In this way, it is possible to validate software models that reproduce the behaviour of the system. Finally, these models can be integrated with prognostic algorithms, which allow the safety of the servomechanism to be increased. Test bench architecture consists of two different modules:

- **Actuation module**
- **Braking module**

Braking module and actuation module are connected with a transmission chain. The actuation module consists of a three-phase PMSM motor by Siemens, which is controlled by a control unit and an inverter that allows switching the phases. There is also a Microbox PC: a PLC that allows controlling the Sinamic S120 AC/AC Trainer Package by Siemens. The motor axis is directly connected to a planeatary Gearbox obtained with FDM (Fused Deposition Modelling). Finally, an encoder is mounted on the gearbox in order to measure the angular displacement.

The braking module consists of a shaft to which a disc is attached. The disc is connected by a servo brake that allows a braking torque to be applied to the rotating shaft. Finally, braking module and actuation module are connected with a transmission chain. In this way it is possible to simulate the action of a braking torque immediately downstream of the electric motor, with the aim of simulating internal friction .

Below is shown a view of the test bench.

Figure 3.1. Test bench

In this thesis an additional module called **load module** has been designed, which allows to apply a load in the form of a moment directly to the gearbox structure, to simulate the action of an external load on the actuation system (for example an aerodynamic load).

3.2 Electric motor

The test bench is equipped with an electric motor SIMOTICS S 1FK7060-2AC71-1CG0 which generates the mechanical power to operate the servomechanism. The motor is a PMSM (Permanent-magnet synchronous motor) with 8 poles and three-phase power supply.

Figure 3.2. Electric motor

This type of motor is also equipped with its own encoder that acquires data on angular position. The general characteristics are reported in Table 3.1-3.2-3.3-3.4, at the end of this chapter.

3.3 Control Unit

The test bench is equipped with a Control Unit CU310-2 PN, made by Siemens.

Figure 3.3. Control unit

The control unit has the task of controlling the motor drive, based on the input commands. Specifically, the control unit receives as input the desired command and rotor position and processes according to the control law the correct switching of phases, which is physically realized by the inverter (Power unit).

For this reason, the control unit is connected to the power unit via a PM-IF interface. The control unit is also connected to the electric motor via a DRIVE CliQ signal cable and to the PC and PLC via an Ethernet connection. Finally, in order to realize a closed-loop control on the servomechanism, the control unit is connected with the encoder installed on the Gearbox.

3.4 Power Module

The power module Blocksize PM240-2 or inverter is the device that has the task of switching the currents on the phases, based on the position of the rotor. In this way, a rotating magnetic field is generated inside the motor, which interacts with the magnetic field of the permanent magnets, making the motor rotate. The frequency with which the inverter switches the phases directly influences the rotation speed of the magnetic field and consequently the rotation speed of the motor.

Figure 3.4. Power module

The power module is powered by AC 380V, and is connected with the control unit, from which it receives commands.

3.5 Microbox PLC

The test bench is equipped with a PLC (programmable logic controller) SIMATIC IPC427E Microbox PC, made by Siemens.

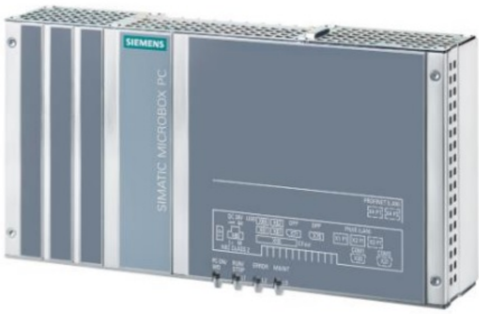

Figure 3.5. Microbox PLC

The PLC runs the TIA software by Siemens, which contains a detailed model of the servomechanism. Through the PLC, a sinusoidal command can be given to the motor, specifying amplitude and frequency. The PLC is connected with the control unit via Ethernet cable and is connected to a monitor that allows the user to operate it.

3.6 Converters

The test bench contains two converters, through which it's possible to transform the voltages to supply the different devices. The first converter transforms from 220V to 24V and is used to correctly power the control unit. The second converter transforms 24V into 6V and is used to power the brake servo of the brake module.

Figure 3.6. Converter

3.7 Planetary Gearbox

A planetary gearbox, manufactured using Fused Deposition Modelling (FDM) technology, is connected to the shaft of the electric motor. Planetary gearbox architecture allows for high gear ratios while maintaining a compact shape, in this way it is possible to increase the torque and decrease the angular speed of the servomechanism. The gearbox has a gear ratio of 124.

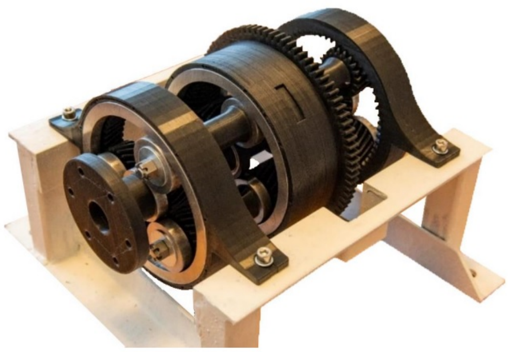

Figure 3.7. Planetary Gearbox

As is shown in Figure 3.8 the gearbox consists of 2 stages.

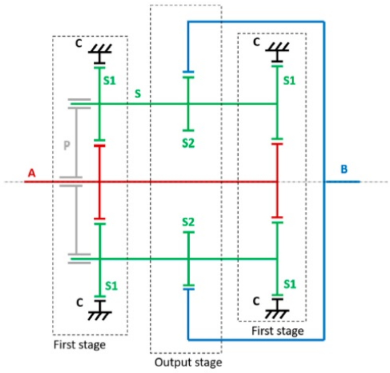

Figure 3.8. Gearbox scheme

Shaft A is connected to the motor and drives the sun gear of the first stage, which is divided into two different ring gears C. Therefore the first stage consists of two ring gears arranged symmetrically at the ends of the gearbox to balance the overall forces. The second stage is the output stage, which is connected to the transmission output shaft B and does not have a sun gear.

3.8 Servo Brake

The test bench is equipped with a servo brake that allows to apply a braking moment directly on the output of the electric motor, before the gearbox.

The disc brake is mounted on a shaft mounted parallel to the electric motor shaft. The motor shaft and the brake module shaft are connected by a chain, which allows the braking torque to be transmitted.

To obtain the appropriate braking torque, the braking module consists of:

- Servo motor Digital Servo DM5163M
- Arduino R3 board
- Load cell

A control law executed by the arduino is used to obtain the desired braking torque. Specifically, when a braking torque is commanded, the arduino commands the position that the servomotor must reach in order to obtain the desired torque.

At the same time, a load-cell, installed on the test bench and connected to the brake servomotor via a 3D printed hinge, measures the force being discharged on the table. Multiplying the force by the distance from the axis of the braking module, the effective braking torque can be calculated. Then the error between commanded braking torque and actual braking torque can be calculated as:

$$error = set - torque. \tag{3.1}$$

In the previous equation "set" is the commanded torque and "torque" is the effective braking torque measured by the loadcell.

The arduino then uses the calculated error as input to a control law code that is based on PI control logic, with a proportional gain and an integrative gain, which allows the steady state error to be cancelled.

3.9 Gearbox encoder

An encoder TSW581HS.M2.5000.5.V.K4.B127.PL10.PP2-5, made by Italsensor company, is connected to the output shaft of the gearbox.

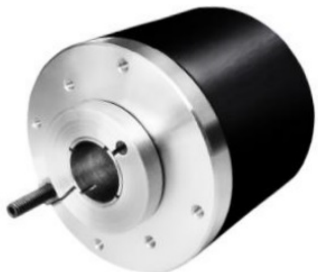

Figure 3.9. Encoder

The encoder makes it possible to measure the angular position of the transmission output shaft, so that closed loop control can be achieved. Specifically, the encoder is connected directly with the control unit that controls the electric motor, so when an input command is given, the control unit compares the actual angular position of the gearbox with the given command and calculates an error and then the motor is commanded in order to cancel it. In this way, the command law is closed.

The encoder is mounted on a micro-mover that allows it to be moved linearly away from and closer to the gearbox crown. In this way a fixed amount of backlash can be simulated. Simulating a backlash on the transmission is useful to evaluate the effects that this can have on the control law and therefore on the entire operation of the servomechanism. Below are reported the data of the electric motor, which powers the servomechanism on the test bench.

Engineering Data	
Rated speed (100 K)	2000 rpm
Number of poles	8
Rated torque (100 K)	5.3 Nm
Rated current	3.0 A
Static torque (60 K)	5.00 Nm
Static torque (100 K)	6.0 Nm
Stall current (60 K)	2.55 A
Stall current (100 K)	3.15 A
Moment of inertia	7.700 kgcm2
Efficiency	90.00

Table 3.1. Electric motor: Engineering data

Physical constants	
Torque constant	1.1 Nm/A
Voltage constant at 20º C	121.0 V/1000*min-1
Winding resistance at 20º C	2.75
Rotating field inductance	30.5 mH
Electrical time constant	11.10 ms
Mechanical time constant	1.75 ms
Thermal time constant	30 min
Shaft torsional stiffness	40500 Nm/rad
Net weight of the motor	7.1 kg

Table 3.2. Electric motor: Physical data

Mechanical Data	
Motor type	Permanent-magnet synchronous motor
Shaft height	63
Cooling Natural	cooling
Radial runout tolerance	0.040 mm
Concentricity tolerance	0.10 mm
Axial runout tolerance	0.10 mm
Vibration severity grade	Grade A
Connector size	1
Degree of protection	IP64
Temperature monitoring	Pt1000 temperature sensor
Electrical connectors	Connectors for signals and power
Holding brake	without holding brake
Shaft extension	Plain shaft
Encoder system Encoder AM24DQI:	absolute encoder 24 bits

Table 3.3. Electric motor: Mechanical data

Optimum Operating point	
Optimum Speed	2000 rpm
Optimum Power	1.1 kW
Limiting Data	
Max permissible speed (mech.)	7200 rpm
Max permissible speed (inverter)	4750 rpm
Maximum torque	18.0 Nm
Maximum current	10.7 A

Table 3.4. Electric motor: limit data and optimum point

Chapter 4

Design of the Load Module

The first step in this thesis, before the installation of the fibers, was the realisation of a load module in order to simulate the action of an external load on the gearbox. In this way, in the test phase it will be possible to evaluate the behaviour of the FBG in the measurement of structural deformations, induced by the external load applied by the load module on the gearbox structure.

Being able to simulate external loads is very important, because in aeronautics the actuators are continuously subjected to external mechanical and aerodynamic loads of varying magnitude. For example, actuators driving moving surfaces must constantly overcome the aerodynamic loads transmitted from the surfaces onto the actuation system. Furthermore, the effects of external loads in aeronautical applications are difficult to measure directly, however knowing them could be very useful for the development of prognostic and diagnostic algorithms. FBG sensors will be used to evaluate the structural deformations induced by the load module on the gearbox.

In this chapter, the load module design and operation are explained in detail.

4.1 Load module Architecture

The technique of additive manufacturing was used for the realization of the mechanical parts of the load module. Therefore, all parts were first designed using Solidworks and then printed by 3D printing with the technique of fused deposition modeling (FDM). The load module consists of a number of different components which together allow a load to be applied in a controlled way. Specifically, it is composed of:

- **Traction Springs**
- **Horizontal mover**
- **Vertical pulleys**
- **Oblique pulley**
- **Winding guide**
- **Wire**
- **Data acquisition system**

The operation of the load module takes advantage of the rotation of the gearbox itself. Two cables are hooked onto the gearbox; when the gearbox rotates, the cables wrap around a guide. The cables on the other end are connected to two springs, which with the rotation of the gearbox are put into tension. The force generated by pulling the springs is transmitted by the cable that wraps around the transmission pulleys and finally discharges onto the gearbox. In this way a torque is transmitted on the gearbox, simulating external loads on the system. To apply a torque the two tension forces that the cables discharge on the gearbox must be in opposite directions. So one cable tensions the gearbox from its top and another tensions in the opposite direction at the bottom. This generates a torque equal to:

$$M = Fd \tag{4.1}$$

In Eq.(4.1) F is the spring force generated by the springs in tension and then transmitted by the cables to the gearbox, d is the winding guide diameter. The cables then wind around a set of pulleys arranged on opposite sides from the gearbox. On the left the group of vertical pulleys acts as a guide for the cable on top of the gearbox, on the right the mover directs the cable below. Both cables are then sent back inside two tubes placed parallel under the test bench, inside which are the two springs. The cables are finally anchored to the springs. When the motor rotates, the cables wind around the guide and the pulleys cause the springs to be tensioned, generating the force needed to obtain torque on the gearbox.

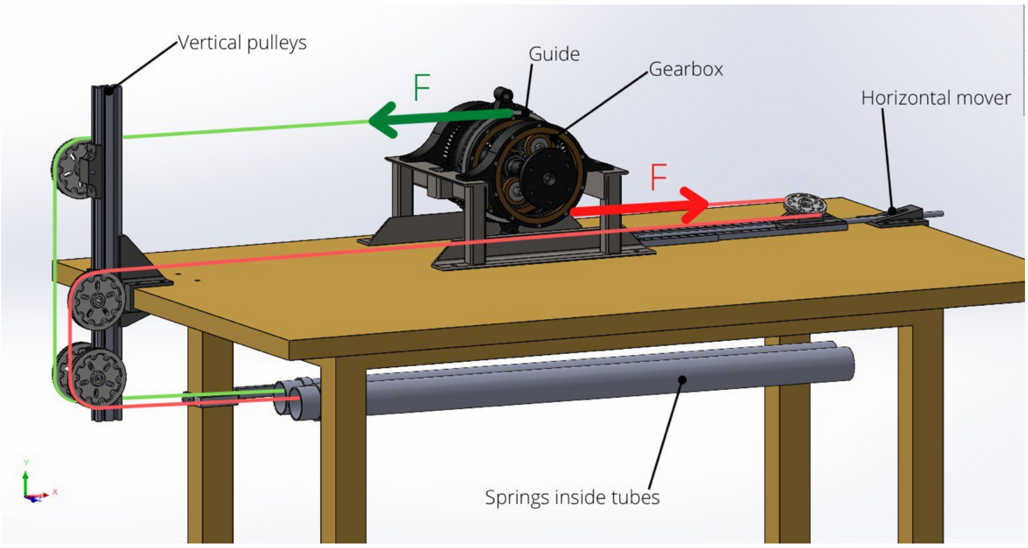

Figure 4.1. Load module architecture

4.2 Traction springs design

Springs are the components that allow torque to be generated. Specifically, the pull of the springs puts tension on the transmission cables, finally the tension of the cables is discharged to the gearbox mounts, so by applying two forces in opposite directions spaced by a distance, the desired torque is achieved. Two identical springs are used, each connected to a different cable. When the motor rotates, the cables wind symmetrically on the guide and pull the springs. The choice falls to springs because it is convenient to have a load as proportional as possible to the rotation of the motor.

The parameters to be determined to fix a spring design are:

- ***d*** *wire diameter*
- ***D*** *mean coil diameter*
- ***L0*** *free length*
- ***n*** *number of coils*
- ***p*** *pitch*

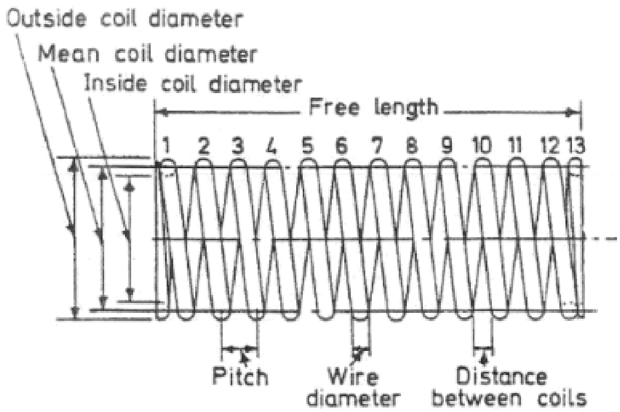

Figure 4.2. Spring design parameters

Very often in extension springs the pitch is equal to the wire diameter, so the coils are all attached to each other. In this way the spring turns out to be much more compact. So in this case we set

$$p = d \tag{4.2}$$

The other design parameters of the spring need to be determined. The load module is designed to apply a maximum torque $M_{max} = 12Nm$ to the gearbox. Considering that the diameter of the rail $d_{rail} = 160mm$ on which the cables are wound, it is derived that each spring under the maximum load condition should generate a tensile force :

$$F = \frac{M_{max}}{d_{rail}} = \frac{12Nm}{0.16m} = 75N \tag{4.3}$$

To be conservative, we consider F=80 N.

Considering the cross section of a coil of the spring, we have that the force F that stresses the spring is divided into a tangential F_t component and one normal F_n to the wire section, as is shown in the figure below.

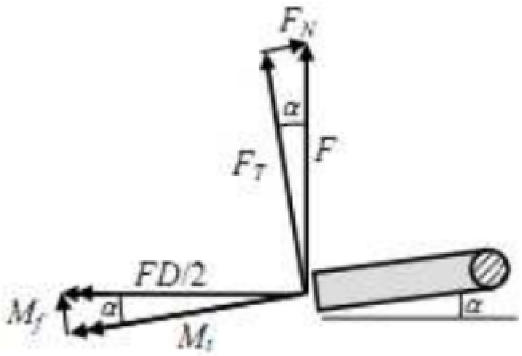

Figure 4.3. Coil section forces

More specifically:

$$F_n = Fsin\alpha \qquad F_t = Fcos\alpha$$
$$M_f = Fsin\alpha D/2 \qquad M_t = Fcos\alpha D/2$$

The normal force and bending moment can be considered zero (F_n=0 and M_f=0), considering the alpha angle sufficiently small. We can then assume that all the force is absorbed in the form of shear, with F_t=F and M_t=FD/2. The value of the shear stress τ at a point on the wire section is given by the sum of two contributions: the stress due to the force F_t and the stress generated by the torque M_t. At the most stressed point of the section the maximum stress can be calculated as:

$$\tau_{max} = \tau_{torque} + \tau_{shear} = \frac{M_t D}{2J} + \frac{F}{A} \tag{4.4}$$

The torque is $M_t = \dfrac{FD}{2}$ and the moment of inertia $J = \dfrac{\pi d^4}{32}$, so the (4.4) becomes:

$$\tau_{max} = \frac{8FD}{\pi d^3} + \frac{4F}{\pi d^2} \tag{4.5}$$

As can be deduced from Eq. (4.5) for a fixed force value F, increasing the outer diameter D increases higher stresses, conversely increasing wire diameter d decreases the maximum stress.

The goal is to find a combination of D and d that in the most critical situation (F=80 N) allows the spring to reach an internal stress that is always less than its yield strength.

Using the Von Mises criterion and assuming that all stresses are shear, it is possible to relate the shear stress τ_{max} to the yield stress $\sigma_{0.2}$ of the steel composing the spring:

$$\tau_{max} = \frac{\sigma_{0.2}}{\sqrt{3}} \tag{4.6}$$

The maximum stress thus calculated is a critical situation, so the formula is divided by a safety factor c=2. This is equivalent to considering a yield stress of the material that is half of the actual yield stress.

$$\tau_{max} = \frac{\sigma_{0.2}}{c\sqrt{3}} \tag{4.7}$$

Substituting (4.7) into (4.5) gives the external diameter:

$$D = \frac{\sigma_{0.2}\pi d^3}{8\sqrt{3}Fc} - \frac{d}{2}[1] \tag{4.8}$$

The spring stiffness K can be calculated as follows:

$$K = \frac{Gd^4}{8nD^3}[1] \tag{4.9}$$

G is the shear module of spring steel and n is the number of coils.

In the case of load module springs, the maximum force they must withstand F=80 N is already known. Then by fixing the value of spring elongation x=1.3 m, it is possible to calculate what the K of the springs must be:

$$K = \frac{F}{x} = \frac{80N}{1.3m} = 0.0615N/m \tag{4.10}$$

The following procedure was followed to determine the design parameters of the spring:

- A value of d is imposed
- D is calculated from the (4.8)
- n is calculated from the (4.9)
- l_0 is calculated as $l_0 = nd$
- All design parameters D, d, n, l_0 are known.

Basing on this procedure a software was developed on Matlab, below is shown the working diagram. Values from UNI EN 10270-1 SM/SH/DH, a steel used for the manufacture of springs, were taken as a reference for yield stress and shear modulus. The following input parameters were included:

- K=0.0615 N/m
- F=80 N
- G= 81500 N/mm^2
- $\sigma_{0.2}$= 1730 N/mm^2
- c=2 (safety factor)

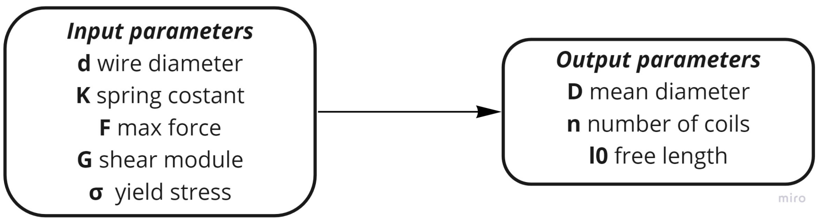

Figure 4.4. Work diagram

The last input parameter to be defined is wire diameter d. To perform a trade off, solutions were calculated for different values of initial d. specifically, d was varied between 2mm and 4 mm. Different values of mean diameter D were obtained in this way. These values are shown in blue in the graph 4.5.

In the graph 4.5,blue points represent the combination of D and d that ensures that the spring structurally resists the applied force, these points are limit points, so the portion of the graph above them represents a spring geometry potentially at risk of failure. In contrast, the points below the blue points are combinations of D and d that ensure the structural strength of the spring. In fact, having fixed the wire diameter d, choosing a lower D than the limiting one is equivalent to having a more elongated spring with a lower D/d ratio and thus a spring that has to bear a smaller torque (M_t=FD/2), on a thicker wire. For these reasons, the following design point was chosen:

- d= 3 mm
- D= 34 mm

This set of d and D guarantees the structural strength of the spring, now it is necessary to calculate the number of turns that guarantees the desired K. In the graph 4.6 the trend of n as a function of K is shown, it is obtained that for the desired K, n=342. Finally, with n=342 it can be calculated that the spring must be long

$$l_0 = nd = 342 * 3mm = 1026mm \tag{4.11}$$

In summary, the following design parameters for the spring were obtained:

- d= 3 mm
- D= 34 mm
- l_0= 1024mm
- n= 342

The springs were made using the spring steel UNI EN 10270-1 SM/SH/DH, also known as C72.

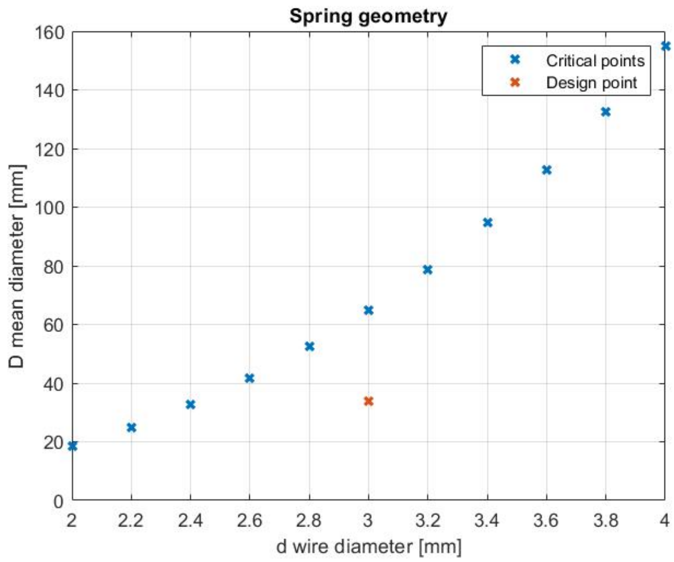

Figure 4.5. D-d relation

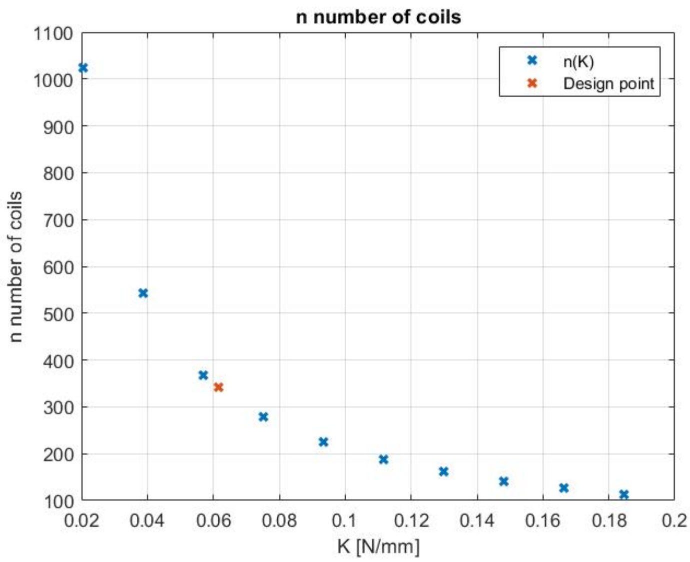

Figure 4.6. Number of coils

4.3 Horizontal mover

The horizontal mover is a system that has the objective of being able to direct the tension of the cable to the lowest hook and close to the table surface, on the gearbox. To achieve this, the system has an oblique pulley anchored on a movable support. The support is not fixed to the table but is anchored on sliding rails. In this way the oblique pulley has a degree of freedom that allows it to move forward and backward relative to the gearbox. The system is moved by the rotation of a handwheel fixed on a threaded rod, the threaded rod passes through the pulley support and screws into a nut embedded in the support. This converts the rotation of the screw into a linear displacement of the system.

The mover makes it possible to add a degree of freedom to the load module. Green arrows in the figure 4.7 show the possible displacements of the oblique pulley. When the motor rotates, the two springs are put in traction and generate the same force because they are subject to the same elongation, which is equal to the circumference described by the guide, but if when both springs are in traction, you turn the handwheel of the mover, you get more or less traction on one of the two springs. Specifically, if the oblique pulley support is moved away from the gearbox, a higher spring tension is obtained, and thus a pure torque is not applied on the gearbox, but a radial force component is also generated, which is equal to:

$$F_{radial} = K\Delta x \tag{4.12}$$

In the (4.12) Δx is the displacement of the mover.

The mover is a system composed of the following components:

- Oblique pulley
- Pulley support
- Fixing support
- Linear guides
- Threaded rod and nut
- Fixing screws and bearings

The horizontal mover always works under traction, all the tensile force is discharged from the cable onto the oblique pulley, which transfers the force to the support that discharges the force onto the nut, as is shown in figure 4.8. The pulley and its support are in fact free to slide relative to the table surface, were it not for the nut in the pulley support and the nuts on the fixed support, which absorb all the forces keeping the rod in tension. When handwheel is rotated, the threaded rod rotates with respect to the pulley support and with respect to the nut that is recessed inside it. The nut is recessed within a hexagonal seat in the support and therefore is not free to rotate, as is shown in figure 4.8. So rotation of the rod with respect to the nut causes a linear displacement of the oblique pulley. The pulley is oblique because of space issues; in fact, above the pulley the braking module is mounted.

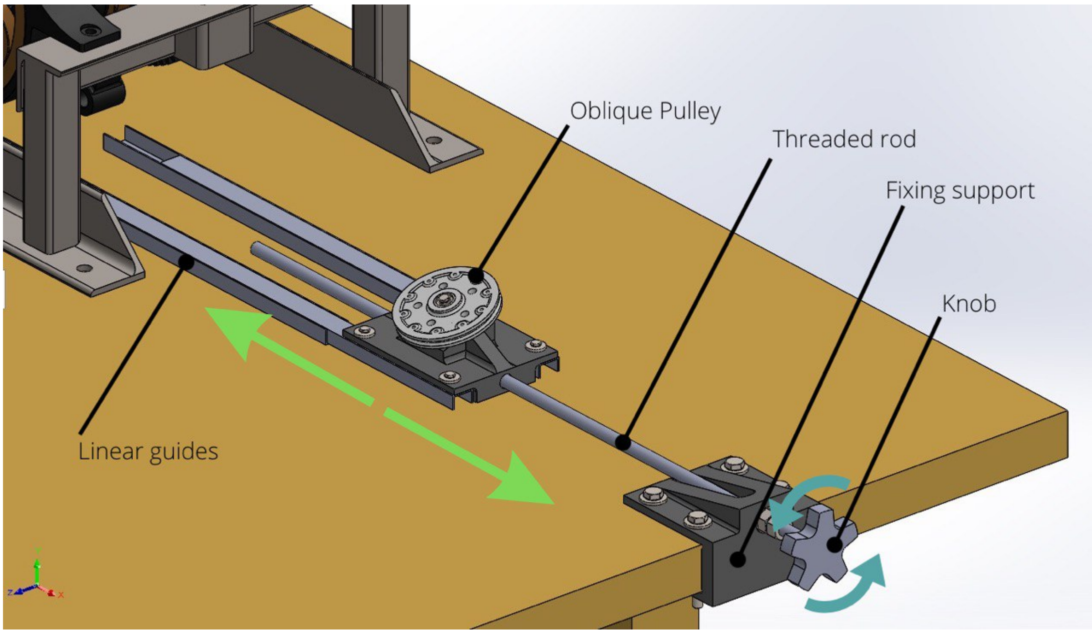

Figure 4.7. Horizontal mover architecture (CAD)

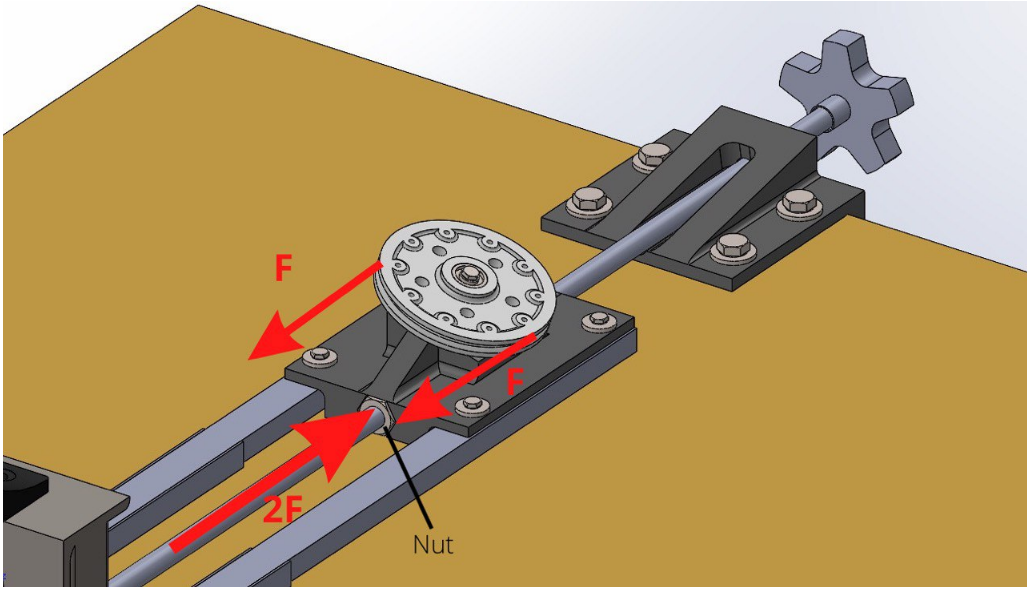

Figure 4.8. Forces on oblique pulley support (CAD)

4.4 Vertical pulleys system

The vertical pulley assembly aims to send both cables back into the tubes containing the tension springs. So both the cable coming from the oblique pulley of the mover and the cable coming from the top of the rail, thanks to the pulleys are rotated 180° and sent back inside the tubes.

The system consists of the following elements:

- Aluminum profile
- C-support
- Sliding supports
- Lower return pulleys
- Middle return pulleys
- High return pulley
- Bearings, nuts and fixing screws.

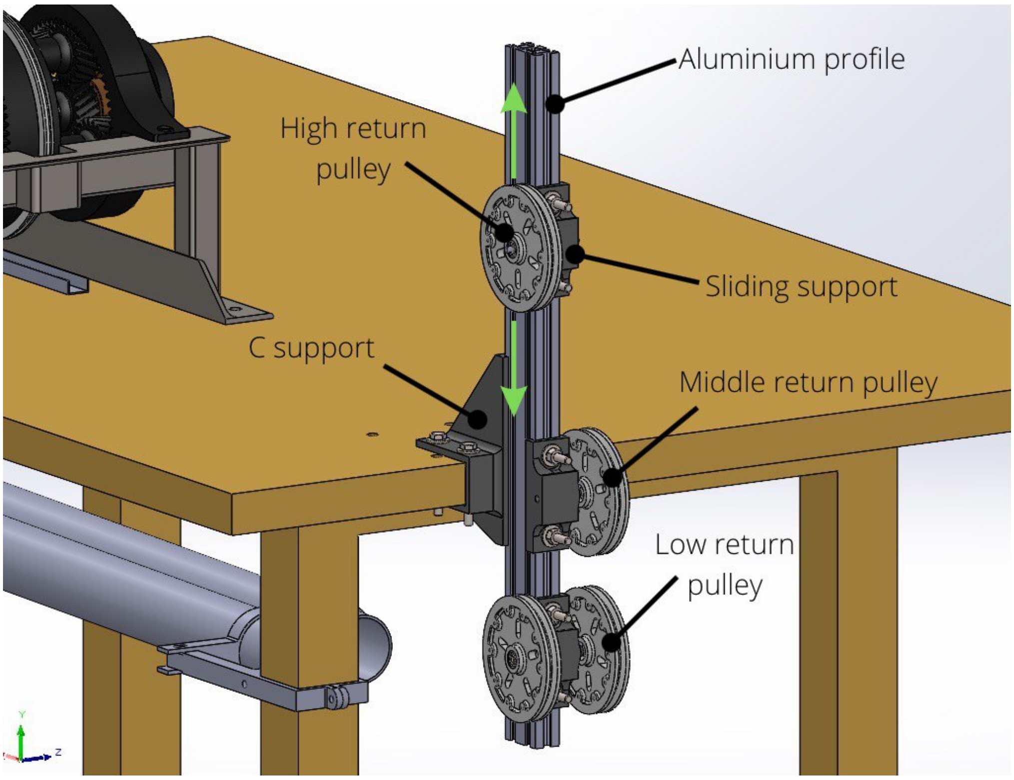

Figure 4.9. Vertical pulley system (CAD)

The top pulley redirects downward the cable coming from the top of the rail, while the middle pulley redirects the cable coming from the horizontal mover. Then both cables are sent back to the low return pulleys that send the cables back into the tubes containing the springs.

All pulleys are attached to an aluminum profile by sliding supports. The aluminum profile in fact contains special grooves to accommodate the heads of the M6 screws, which attach the sliding supports to the profile. This makes it possible to move the pulleys vertically. In particular by moving up or down the pulley at the top, it is possible to achieve over-tensioning on one of the two springs, thus inducing a radial force on the gearbox, just as happens with the horizontal mover. Shielded miniature ball bearings with an outer diameter of 13mm and an inner diameter of 4mm are used on all pulleys. Because of the shielding, the bearings are better protected from dirt and grease and last longer.

The sliding mounts have a hole to accommodate an M4 threaded rod that supports the pulleys and allows them to rotate. Self-locking nuts were used to attach the pulleys to the threaded rod, so as to prevent them from unscrewing as the pulleys rotate. All sliding supports are identical except for the lower one. The lower support in fact supports the two lower pulleys. In this case, the axis of rotation of the pulleys and thus the axis of the threaded rod is tilted 2° from the axis of rotation of the upper pulleys. This choice was made to grant a slight inclination to the tubes containing the springs, which otherwise would have generated interference with the table foot. All of the forces generated by tensioning the cables are discharged onto the pulleys and thus onto the profile, which is attached to the table via the C-bracket. The C-bracket is therefore the most stressed component in structural terms. It has two ribs both below and above the table surface, which enable it to support the torque generated by the profile. The system is not automatically in equilibrium, as the force of the upper pulley possesses a larger arm than the other pulleys and thus generates a torque. This moment is absorbed by the C-shaped support, which in fact has a strengthening rib at the top to the table surface. The profile is attached to the c-support by two M6 screws, one placed in the top rib and one in the bottom rib of the support. In this way, the top rib absorbs loads by compacting, the bottom one by working in tension.

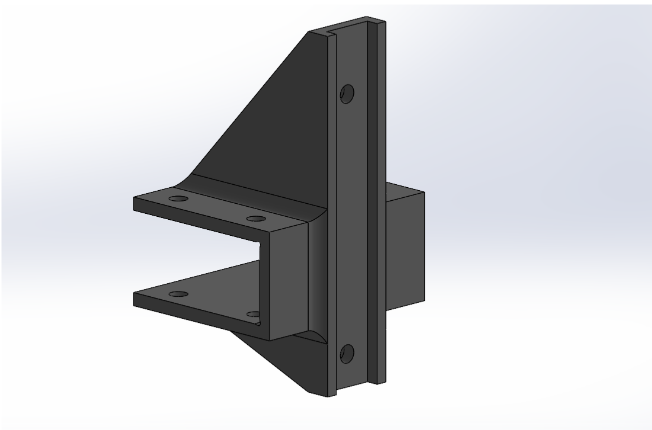

Figure 4.10. C-support (CAD)

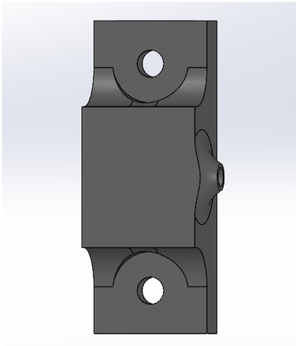

Figure 4.11. Sliding support (CAD)

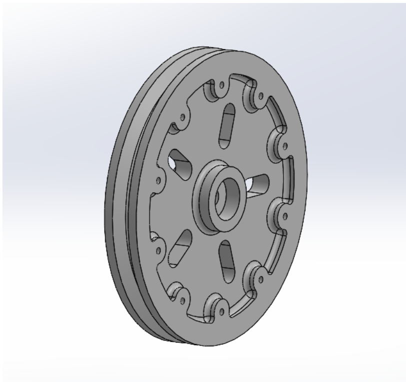

Figure 4.12. Pulley (CAD)

4.5 Winding Guide

The guide is used to allow the cables to wrap neatly around the gearbox as it rotates and the springs are put into traction. The guide consists of two half-conferences that were then joined and installed on the gearbox, going to form a circular guide that allows the cables to be wound. The two components were glued to the gearbox surface using cyanoacrylate-based glue. The throat housing the cables was sized by multiplying the diameter of the cables by a factor of 5. Thus given the diameter of the cables equal to 0.8 mm, a throat equal to 4mm was designed. The geometry of the guide is shown in the figure 4.13.

The cables used are 0.8 mm thick nylon cables, capable of withstanding a maximum tensile strength of 20 kg, thus more than twice the maximum tensile strength the system is designed to withstand, which is 8.15 kg (80N). The cables were wrapped around the rail and then tied to the eyelet mounts on the gearbox.

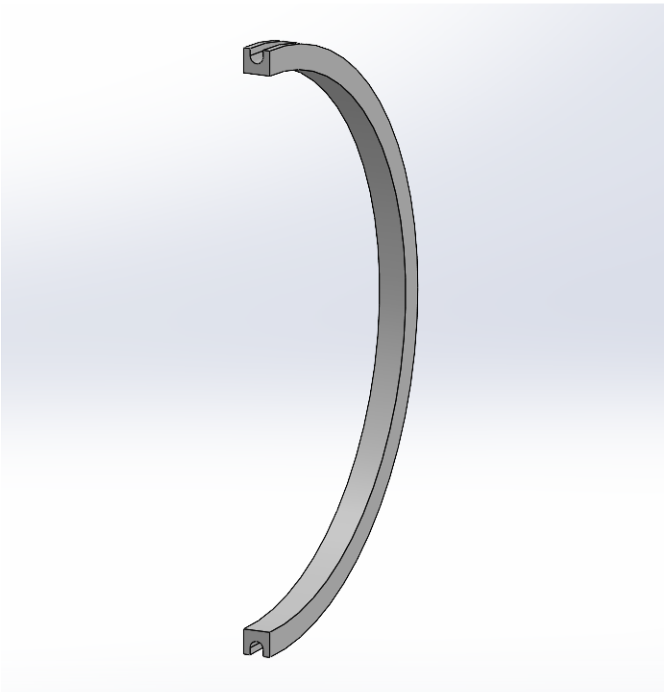

Figure 4.13. Guide (CAD)

4.6 Data acquisition system

The acquisition system aims to acquire in real time the load in the form of torque that the load module is applying to the gearbox. The system takes advantage of the use of two loadcells HX711 that constantly measure the tensile force generated by the springs. The torque generated on the gearbox is then calculated as: follows:

$$Torque = (F_1 + F_2) * r \tag{4.13}$$

F_1 and F_2 are the forces generated by the two springs inside the tubes and r is the guide radius. Loadcells are powered by 5V drive voltage and are installed on a panel on which the tubes containing the springs are embedded. The panel contains two holes through which cables run that connect each loadcell to its respective spring. In this way the loadcells provide the tensile forces F_1 and F_2 to which the springs are subjected, thanks to 24 high precision A/D converter chip hx711. The loadcells are connected to an arduino that acquires data and processes it.

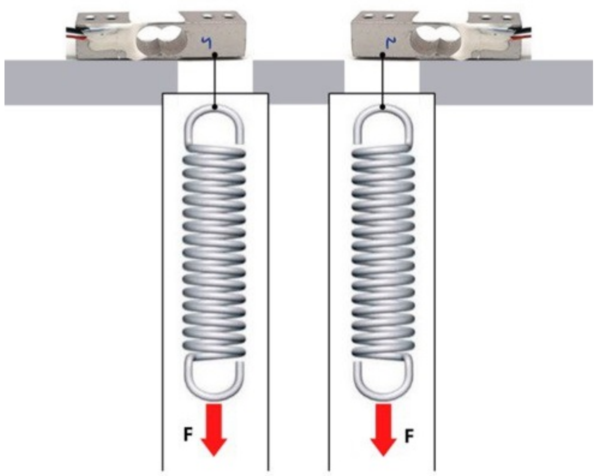

Figure 4.14. Data acquisition architecture

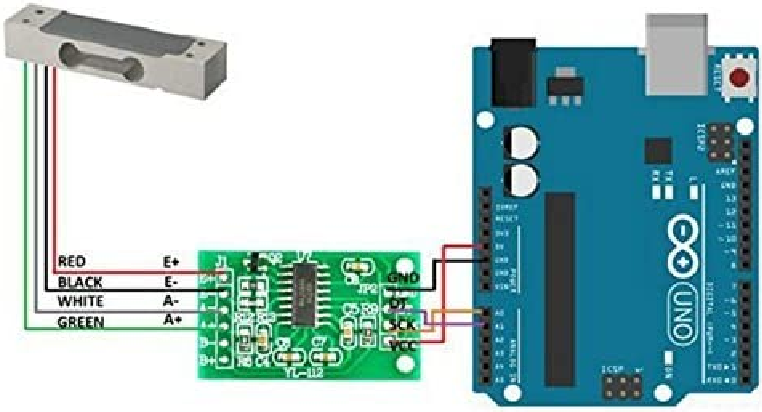

Figure 4.15. Data acquisition hardware

Chapter 5

Installation of FBG sensors and strain gauges

The thesis project continues with the installation of the FBG sensors on the Gearbox to evaluate their operation and reliability in measuring mechanical deformation when an external load is applied to the Gearbox via the Load module.

With a view to calibrating and evaluating the behavior of FBGs in measuring structural deformations, it was decided to install strain gauges on the Gearbox as well, so it's possible to compare the data collected by both types of sensors, which exploit different physical principles and acquisition systems.

Both types of sensors measure the same physical quantity namely structural deformation, however, FBG have some features that make them very useful for diagnostics and prognostics. One of the advantages of FBG is that they can be installed in series on the same fiber, so with a single cable it is possible to acquire data on multiple points of the structure, optimizing in terms of weight and complexity.

Equipping a servomechanism with FBG can be useful for doing structural monitoring. FBGs are also sensitive to changes in temperature, which are often a signal of certain malfunctions such as short circuits in the motor coils or excessive friction.

The installation of FBGs on the structure to be monitored is a very important aspect concerning the quality of the data obtained. FBGs are fragile sensors that require care during installation.

This chapter explains the installation of the sensors, which in this case required the development of an ad hoc procedure for FBG, due to some design complexities that will be explained later.

5.1 Installation points

The first step before the installation of strain gauges and fibers was to choose the number of sensors and the location in which to install them. Since a torque is applied on the gearbox via the load module, it was chosen to apply the sensors (FBGs and strain gauges) at the mechanically most stressed points of the structure.

The Gearbox is anchored to a steel stand by 4 fastening screws. The screw holes are located on an extension of the Gearbox's outer crown. For structural reasons in the design of the Gearbox, edgy surfaces were minimized, so the part of the Gearbox that houses the holes is connected to the outer crown through concave geometry.

In the concavities near the holes is likely where the greatest mechanical deformations are obtained when external torque is applied to the gearbox. This is true because it is precisely at the point of contact between the gearbox and steel support that the constraining reactions are concentrated to counteract the applied external torque. Therefore, it was chosen to install sensors at these 4 points to maximize the measurement of load-induced deformation.

For each concavity, 1 FBG and 1 strain gauge were installed in pairs, in close position. A total of 4 FBGs and 4 strain gauges were installed. Having strain gauges and fibers applied at the same points makes it possible to compare the results obtained during acquisition, so it is possible to calibrate the FBGs and generally evaluate their behavior in measuring strain in the static regime or, for example, vibration in the dynamic regime. A representation of the points chosen for sensor application is shown in figure 5.1.

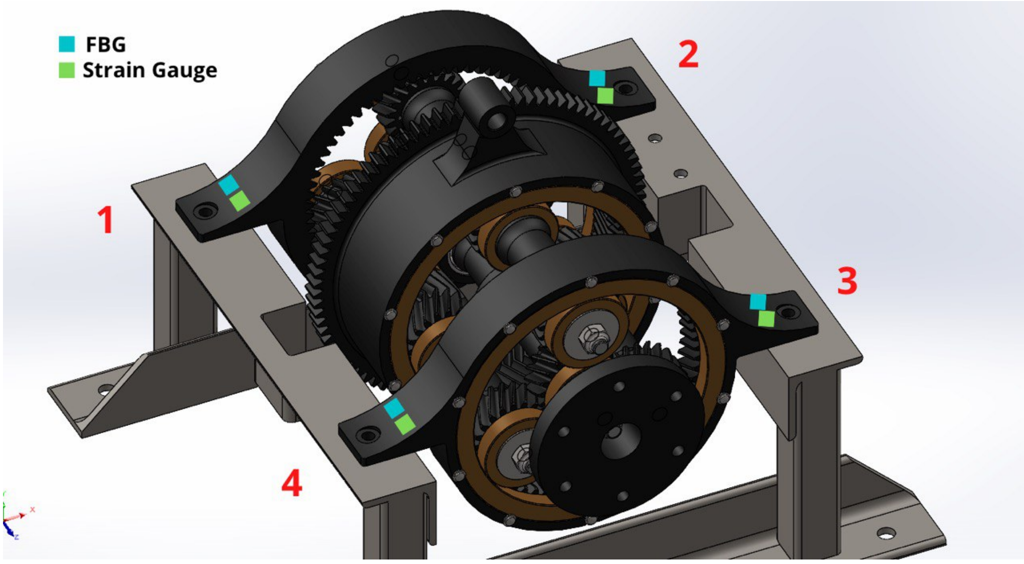

Figure 5.1. Sensors installation points

Ideally it would be optimal for strain gauges and fibers to be installed in the exact same place, however for practical reasons this turns out to be complicated. In fact, gluing the FBG on top of the strain gauge (or vice versa) presents practical difficulties and creates a thick layer of glue that does not adhere the upper sensor to the Gearbox surface, making strain measurements inaccurate. In fact, the glue has different mechanical properties from the PLA of which the Gearbox is constructed and is therefore subject to different deformations.

For all these reasons, it was chosen to install FBGs and strain gauges adjacent but not one over the other. The sensors were then installed slightly away from the screw holes to prevent mechanical deformation from being too much affected by the presence of the screw hole.

The sensors were numbered from 1 to 4 as shown in the figure 5.1 so that they could be distinguished during the data acquisition phase.

5.2 FBG installation

The locations chosen for the installation of the FBGs and strain gauges are optimal in terms of mechanical stresses, but the surfaces are curved, making fiber installation difficult. Generally, fibers are more accurate in measuring strain if they are glued pretensioned. When fibers are bonded to a flat surface, mechanical tensioners can be used to tension the fiber before bonding it.

In this specific case, using tensioners is impossible, both because of the available spaces on the test bench and because the installation surface is curved. Therefore, an alternative method of tensioning the fiber and adhering it to the surface had to be evaluated. Specifically, the idea was to use supports that are the geometric negative of the concavity of the gearbox.

5.2.1 Negative parts

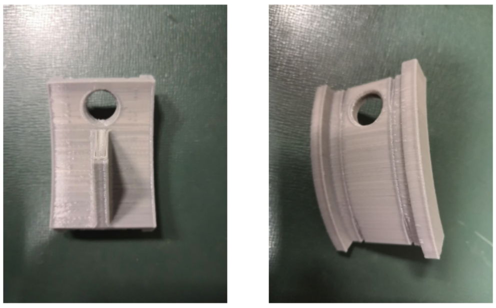

Figure 5.2. Negative parts

Negative parts are designed to be able to draw the fiber and make it adhere to the curved surface, before gluing it.

Negative parts were designed on Solidworks and 3d printed using PLA. Grooves were inserted in the bottom part to allow the fiber to sit inside and not be overstressed in shear when the negative part is pressed onto the gearbox. A hole was added so as not to generate interference with the screw that attaches the gearbox to the steel stand and a triangular extrusion to allow for handling and positioning of the part.

5.2.2 FBG Installation procedure

Then the succession of actions performed to arrive at fiber bonding are listed and discussed.

Fiber preparation

1. A heat-shrink sleeve was applied to the fibers to make it more durable during installation and prevent accidental breakage. The sheath was installed in the part between the connector and the FBGs, so that the fiber can be handled more safely when connecting it to the interrogator.

2. The end of the fiber without FBG was removed to shorten the fiber and facilitate installation.

Fiber installation

1. The Gearbox surface is cleaned before fiber application so that dust can be removed.

2. The fiber is connected to the interrogator via the connector, so its proper operation can be evaluated before installation and tensioning can be monitored in real time.

3. The FBG needs to be tensioned, so a small section of fiber preceding the Bragg is glued to the gearbox, this way when the glue has dried it will only be necessary to pull the fiber to one side, as the glue will bind the fiber to the gearbox, keeping the tension applied.

4. When the glue has dried, the fiber is manually put into tension. On one side of the bragg the operator applies a force, on the other side the glue maintains the pull. At this stage the bragg is tensioned but not resting on the curved surface of the gearbox, the tension in fact keeps it suspended, as is shown in figure 5.3.

5. The manually applied tension is monitored in real time via a PC connected to the interrogator, so the actual tensioning of the fiber can be evaluated. Tensions were applied which caused an increase in wavelength of about 2nm.

6. An interface material is added to the negative component on which the fiber will lie, to prevent the component from sticking to the gearbox and cannot be removed.
7. Cyanoacrylate glue is placed on the gearbox at the exact spot where the Bragg should be installed.
8. The negative component is placed on top of the tensioned fiber, and the fiber is inserted inside the special groove on the component.
9. The negative is pushed toward the concavity of the gearbox, until the bragg is pressed onto the glue arranged below, as is shown in 5.4.
10. The pressure is maintained for 5 minutes to allow the glue to dry.
11. The negative component is removed and the FBG is found to be glued in the desired position.

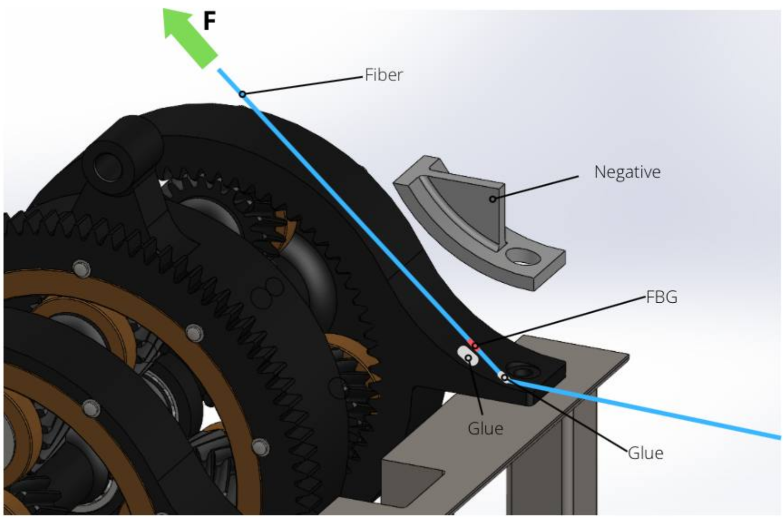

Figure 5.3. Procedure FBG installation (1° Phase)

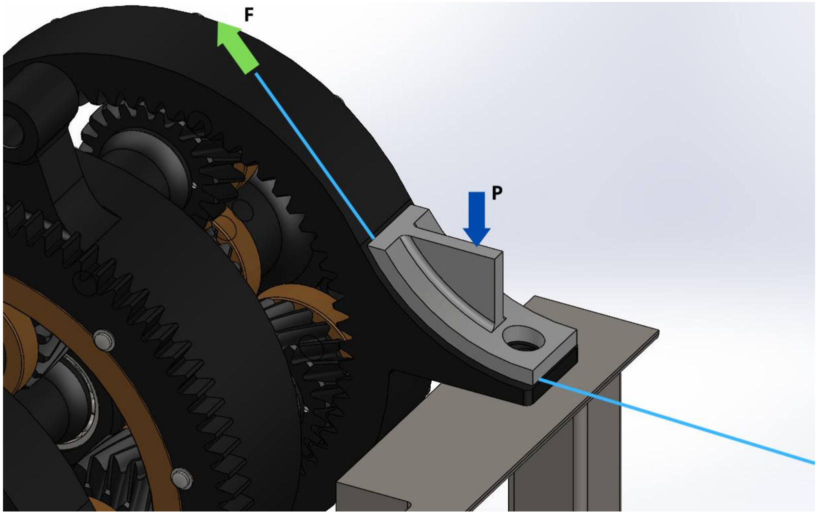

Figure 5.4. Procedure FBG installation (2° Phase)

5.2.3 FBG Installation difficulties

Fiber installation presented difficulties due to the fact that curved surfaces make tensioning and bonding complicated. Thanks to the procedure used, all fibers were installed in the desired position and with a certain level of tensioning. However within a few minutes of bonding the FBGs slowly lost tension until they lost all the tension given to them at the beginning. Thus the FBGs were tested in a non-tensioned state.

The loss of tension in the minutes after installation is probably attributable to the settling of the glue and the glue-PLA interface. Although the glue is almost completely dry it goes through a settling phase during which the fiber gradually loses tension.

Another complexity is related to the fact that fiber is a brittle material, so high care must be taken during the bonding stage. The fiber could break if overstressed in shear, for example by exerting too much pressure through the negative component. At the same time, exerting tension manually on the fiber does not achieve forces comparable to those achievable with tensioners. In addition, care must be taken when tensioning to apply a force in the correct direction, otherwise shear stresses may be applied that can lead to FBG rupture.

FBGs can be installed on the same fiber or on different fibers. When FBGs are installed on the same fiber more care must be taken. In fact, if FBGs on the same fiber are not installed at the same time, the possible rupture of one of them can also compromise the second FBG in series. in fact, the signal travels on the same channel and the rupture of one FBG results in the complete shearing of the fiber.

5.3 Strain Gauge installation

The strain gauges were installed subsequent to the FBGs. Time was given for the glue of the FBGs to be able to dry and settle. This choice was made because bonding strain gauges is easier and does not require negative components. However, soldering of the pads is required after bonding, and compared with FBGs, many more cables are required (2 each strain gauge).

5.3.1 Strain Gauge overview

The electrical resistance strain gauge is an instrument used to measure the dimensional deformation of a body on which it is installed. The strain gauge consists of a very thin conducting metal wire installed on a plastic material.

When the body on which it is installed undergoes deformation, the wire lengthens or shortens in proportion to the deformation. By connecting a Wheatstone bridge to the strain gauge terminals, the change in electrical resistance can be measured and traced back through it to the strain. The increase in wire strength is proportional to the strain through a G_f factor called Gauge factor, expressed by the following equation:

$$G_f = \frac{\Delta R/R}{\Delta L/L} \tag{5.1}$$

G_f value is typically around 2[2].

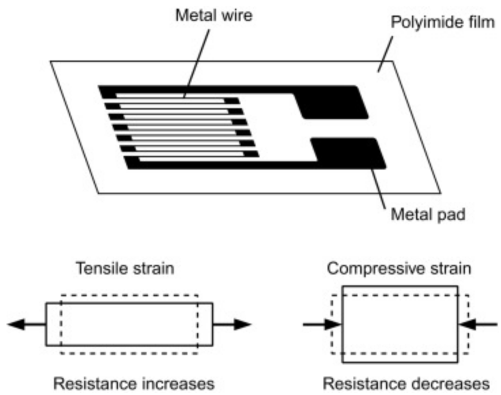

Figure 5.5. Strain Gauge Scheme

5.3.2 Strain gauges installation procedure

The following procedure was followed to install the strain gauges:

1. Once the strain gauges were removed from the casing, they were cleaned to avoid the presence of dust.

2. The Gearbox surface near the fibers was cleaned. This operation is necessary to remove dust and especially possible residue from the glue used for the fibers.

3. The strain gauge is placed on tape so that it can be handled carefully and positioned at the desired location.

4. The strain gauge is placed at the desired location.

5. The tape is lifted from one end and folded back on itself so that glue is placed on the surface of the strain gauge. Cyanoacrylate glue is used.

6. The strain gauge is placed in position and pressure is applied to make it adhere to the surface of the gearbox

7. Pressure is maintained for 5 minutes, after which the tape is removed, to allow the glue to dry

8. Strain gauge pads are cleaned .

9. The leads are soldered to the strain gauge pads using a tin alloy.

10. A layer of polyurethane-based protective material is applied to the strain gauge

11. The strain gauge is connected to the acquisition unit to verify proper operation.

5.3.3 Strain gauges installation difficulties

Strain gauges are more maneuverable during installation when compared to FBGs, which is also why it was chosen to install them later so that more operational space is available for the fibers. However, once glued, the terminals must be connected to the cables, and this operation can be complicated if done in an operationally inconvenient location with little space available.

In the case of the gearbox also, the use of the tin soldering iron is made complicated because of the base material (PLA): when working on PLA-based surface such as the gearbox, care must be taken not to bring the soldering iron close to the surface to avoid melting the plastic and altering the mechanical properties or worse the functionality of the component.

Finally from the point of view of link management, the strain gauges added a total of 8 cables (2 per strain gauge) to the Gearbox, as opposed to the fibers, which required only 3 cables, so it was necessary to direct them appropriately to prevent them from interfering with the operation of the Gearbox.

5.4 Installation results

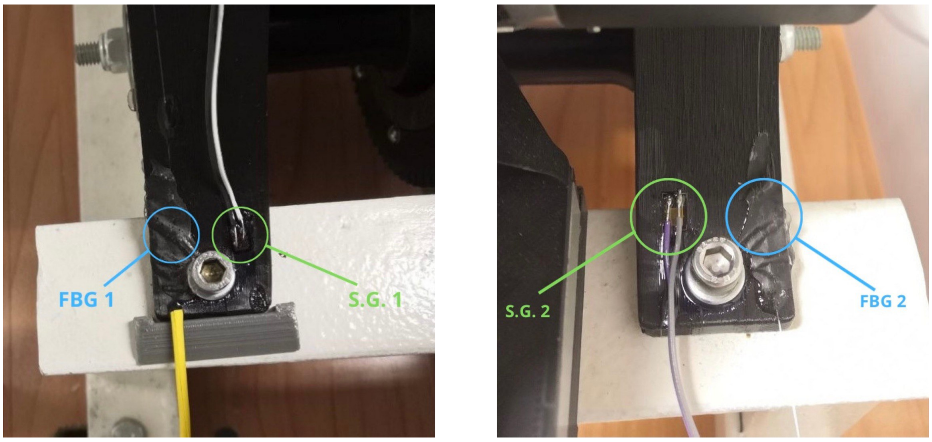

Figure 5.6. FBG and Strain gauges in positions 1 and 2

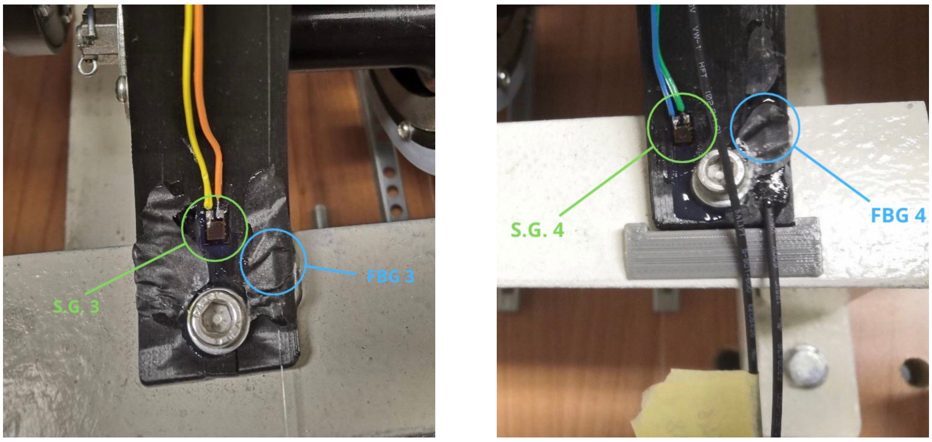

Figure 5.7. FBG and Strain gauges in positions 2 and 3

The photo shows the 4 pairs of sensors installed at the 4 pre-set points of the gearbox. The FBG1 and FBG2 sensors were mounted on the same fiber. The fiber was arranged on the gearbox's cinrconference arc, so the relative distance between the Braggs was fixed by design before the fiber was made, so that they coincided with their respective installation points. FBGs 3 and 4, on the other hand, were mounted separately and are therefore each equipped with their own connector, for data acquisition with the interrogator.

Note that Strain Gauge 3 was not mounted on the same transverse axis as the FBG but slightly higher and centred with respect to the screw. This is because, due to a previous gluing attempt, it was not possible to install the strain gauge next to the screw and on the same axis as the FBG. It was decided to apply the sensor anyway in order to be able to assess how this deviation in position affects the results of subsequent measurements.

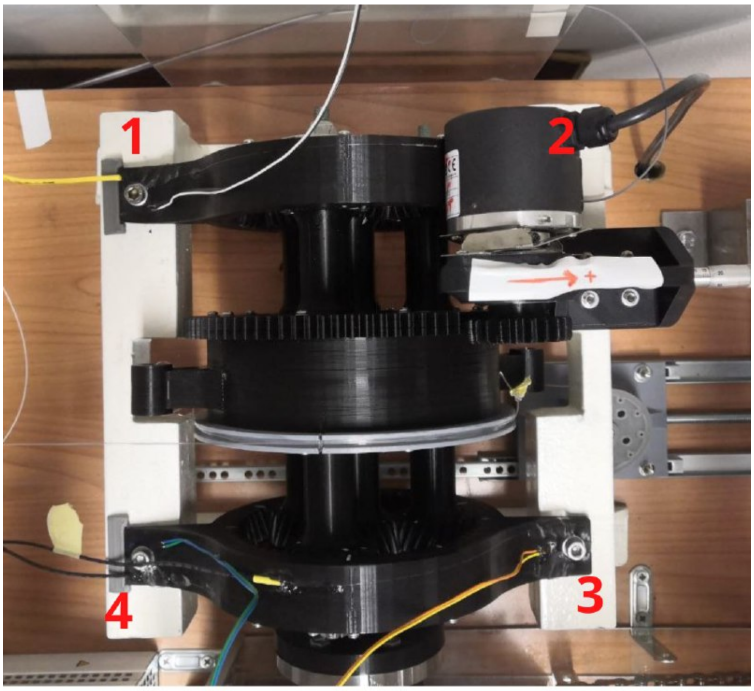

Figure 5.8. Sensors numeration

Channel/Fiber	**FBG**	**Wavelength**
1	FBG 1	1546 nm
1	FBG 2	1538 nm
2	FBG 3	1538 nm
3	FBG 4	1555 nm

Table 5.1. FBG Wavelengths

Chapter 6

Experimental tests and Results

After the installation of the load module and strain measurement sensors, the experimental tests were carried out. The objective of the tests is to apply a torque to the Gearbox via the Load module in order to simulate an external torque downstream of the servomechanism. At the same time, strain gauges and FBGs are used to monitor the structural deformations of the Gearbox under load application. The aim is to verify the behaviour of the FBGs in the transient and steady-state phase and, if necessary, to calibrate them, which is made possible thanks to the data acquired by the strain gauges. In order to achieve the external load, the gearbox must be set into rotation by the electric motor, the rotation of the gearbox allows the cables of the load module to wrap around the rail and at the same time put the springs into tension. The tension generated by the springs is discharged onto the gearbox via the cables and generates a torque that increases linearly with the rotation of the gearbox. The torque finally causes a deformation of the gearbox structure, which is measured thanks to the installed set of strain gauges and FBGs.

In order to obtain a data set that allows the results to be appropriately analysed, the following actions must be carried out simultaneously during the tests:

- Input commands to the motor.
- Acquisition of strain gauge data.
- Acquisition of FBG data.
- Acquisition of load-cell data related to the load module, to measure the applied torque.

In order to carry out these actions, the test bench layout set out in Chapter 3 and Chapter 4 was modified appropriately. Specifically, the interrogator for acquiring FBG data and the acquisition unit for acquiring strain gauge data were added.

In this chapter, the procedure used to carry out the tests will be explained in detail, followed by an explanation of how the various tests are differentiated, and finally, the results obtained will be presented and commented.

6.1 Test bench layout

The load module, the interrogator for FBGs and the strain gauge acquisition system were added to the test bench set out in Chapter 2.

Two PCs, (PC1 and PC2) are used to perform the tests. PC2 is used to acquire fiber data and is connected via Ethernet to the interrogator, PC1 is used to give commands to the motor via Ethernet and to acquire data from the Load module via USB, which is processed by the arduino UNO.

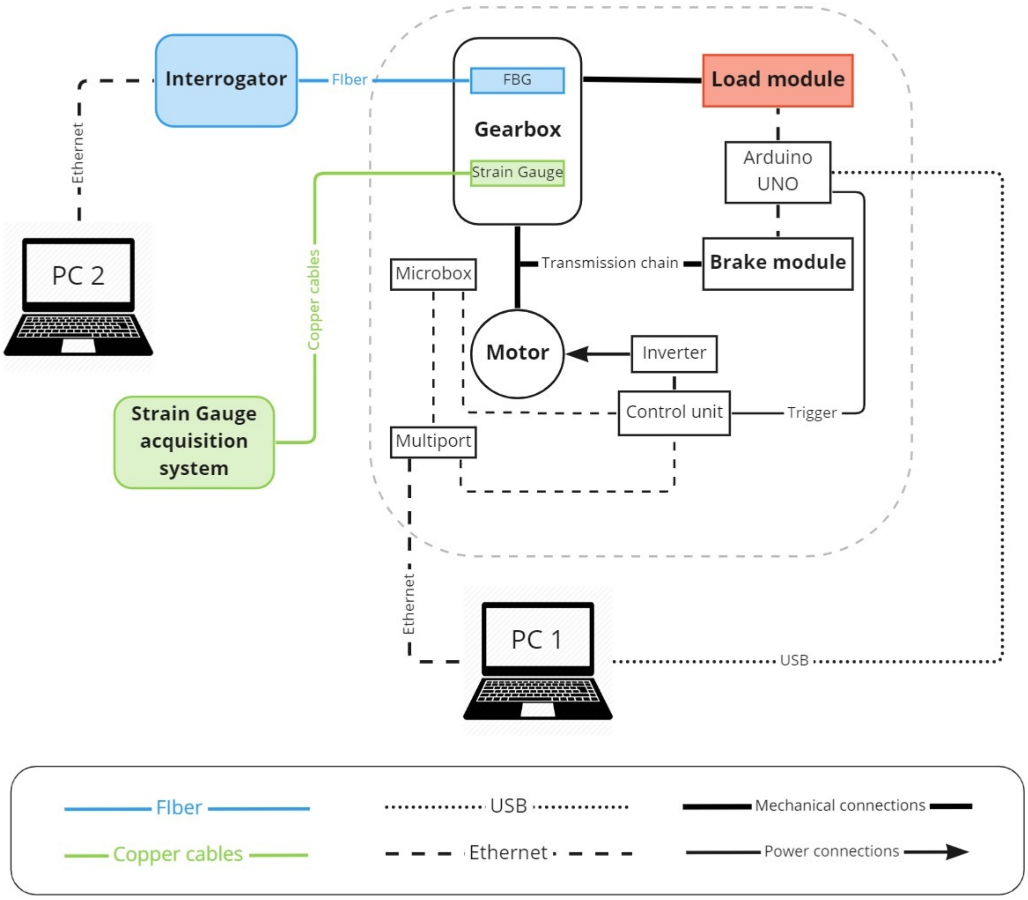

Figure 6.1. Test bench layout

6.1.1 Interrogator

The fiber data acquisition system is based on the use of an optical interrogator. The fiber cables on which the Braggs are installed terminate with a connector that allows the fiber to be connected to the interrogator. The model "SmartScan" from the Smartfiber company was used for testing. The interrogator emits a frequency modulated laser signal within the fiber with a narrow band, then the signal reflected by the bragg is sent to a photodiode. The photodiode is finally connected to a transimpedance amplifier, which converts the current into an analogue voltage that is proportional to the optical power and the frequency of the reflected signal. Finally, The signal is converted to digital and displayed. The interrogator can simultaneously analyse 4 optical channels, so it has 4 different connections for optical connectors. In total, it can simultaneously analyse a maximum of 16 FBG sensors, using a scan frequency of 2.5 Khz. The interrogator can analyse a frequency range of 40nm (1528 - 1568 nm), so all frequencies of the Braggs installed on the same fiber must be within the 1528-1568 range and be sufficiently spaced to allow the reflected signal at each Bragg to be distinguished. The interrogator processes sensor data and transmits it to a PC via an Ethernet connection. Smartfiber's own 'smartsoft' software was used to obtain the results. The software allows the selection of the number of connected channels and sensors, the setting of acquisition frequencies, transmission frequencies and processing rates.

Figure 6.2. Smartscan interrogator

Figure 6.3. FC connector

Smartscan interrogator	
Measurement and Processing	
Wavelength Range	40 nm (1528-1568 nm)
Number of Optical Channels	1,2,3,4
Maximum Number of Sensors/Channels	16
Scan Frequency (all sensors simultaneously)	2.5 kHz
Maximum Scan Frequency	25 kHz
Repeatability	<1 pm
Wavelength Stability	<5 pm over temp. range +/- 20 pm
Dynamic Range	27 dB
Dynamic Range	37 dB
Gain control	9 levels per channel or per sensors
Onboard Processing	For conversion of measuring units and interfacing to client systems
Bragg Grating Full Width Half Maximum (FWHM)	Minimum > 0.2 nm, > 0.5 nm
Environmental and Electrical	
Dimensions	140 x 115 x 85 mm
Weight	0.9 kg
Operating Temperature	-15 to +55 °C
Comms Interface	Ethernet (UDP-IP)
Optical Connector	FC/APC
Input Voltage	+9 to +36 VDC

Table 6.1. Smartscan Specifications

6.2 Test Procedure

The following procedure was followed to perform the tests.

6.2.1 Test bench preparation

1. PLC and the monitor connected are switched on.
2. Control-Unit is switched on.
3. PC1 is connected via Ethernet to the multiport connected to the microbox and the control unit. This allows data to be acquired from the control unit

and commands to be sent to the motor.

4. The PC1 is connected to the arduino via USB connection, to acquire data from the Load module.

5. PC2 is connected to the interrogator via Ethernet.

6. Strain gauges are connected to the acquisition unit.

7. The test bench is powered by 380V.

6.2.2 Data acquisition

1. PC1 checks that the springs are in a resting condition and therefore that there is no load applied on the gearbox.

2. From PC2, the correct reading of all FBGs and their respective wavelengths is verified.

3. The correct reading of the strain gauges is verified.

4. The motor position is reset.

5. The command to be applied to the motor is selected and pre-loaded.

6. Strain gauges are reset.

7. Strain gauge data acquisition from acquisition unit is started.

8. FBG acquisition from PC2 is started, using "Smartsoft" software.

9. Run of Matlab programme acquiring load cell data on PC3.

10. Verification of effective serial communication between PC3 and arduino.

11. The command is applied to the motor via PC2.

12. Data are acquired until the commanded end position is reached.

6.3 Test Execution

Several tests were carried out to obtain a torque on the gearbox and measure the deformations. Each test is divided into two consecutive stages:

1. **Load phase:** A step position command is given as input to the motor. As the motor reaches the commanded position, the cables wrap around the gearbox and the springs are put into tension, generating an external torque on the gearbox, which increases progressively during the transient. When the gearbox reaches the commanded position, the motor stops and the gearbox remains loaded with a static external torque. Throughout the phase, strain gauges and FBGs measure deformations.

2. **Unload phase:** A step command equal in modulus but opposite in direction to that of the load phase is given to the motor. Before the command is executed, the gearbox is subjected to a torque, because the springs are in tension due to the load phase that has just occurred. As the gearbox reaches the commanded angular position, the springs unload proggressively until they reach the rest condition, which coincides with no external load applied on the gearbox. Throughout the phase, strain gauges and FBGs measure deformations.

Both the loading and unloading phase have this structure:

1. **Initial load:** The motor has not yet received the command so the load is constant. The initial load is zero for the loading phase and non-zero for the unloading phase.

2. **Transitional load:** The motor is reaching the commanded position so the external torque evolves over time in both the unloading and loading phases.

3. **Final load:**The motor has reached the commanded end position and therefore the gearbox is subjected to a constant load. The end load is zero in the unloading phase and non-zero in the loading phase.

A total of six different tests were carried out. Each test differs from the others in the size of the control commanded to the motor and consequently the load applied. So in all tests, a step command was given as input to the motor, but the final commanded position is different.The tests performed are summarised below in the table.

Test	Type of command	Command (Load phase)	Command (Unoad phase)
1	STEP	+30 deg	-30 deg
2	STEP	+40 deg	-40 deg
3	STEP	+50 deg	-50 deg
4	STEP	+60 deg	-60 deg
5	STEP	+70 deg	-70 deg
6	STEP	+80 deg	-80 deg

Table 6.2. Performed Tests

6.4 Post-processing

All data collected during the tests were post-processed in the Matlab environment. A software was developed that performs the following actions:

- **Data reading and saving:** All data from load-cells, FBG, strain gauge and control-unit are saved in Matlab Workspace.
- **Data Interpolation (FBG-strain gauges):** The data acquisition of FBGs and strain gauges takes place with two different acquisition systems, which have different data acquisition frequencies. Specifically, the interrogator saves data at 100 Hz, while the strain gauge saves data at 50 Hz, so there is less data on the strain gauges over the same time interval. Furthermore, the FBG and strain gauge acquisitions have different durations and are not synchronised in time, as they are started one after the other. Then the software makes the duration of the acquisitions the same, synchronises the acquisitions in time and interpolates the strain gauge data into the fiber time, so that the same amount of data is available every time interval.
- **Data comparison (FBG-strain gauges):** In all tests performed, data acquired by FBGs and strain gauges are compared. The programme calculates

a number of physical quantities and draws up graphs, which enable the strain data from the FBGs and strain gauges to be compared in both static and transient phases. FBG and strain gauges data acquired are then compared with those of the control-unit.

6.5 Results

The following section will present the results obtained from the post-processing of the data. The main objective is to verify the behaviour of the FBGs in static and dynamic regimes and to calibrate the FBGs on the basis of the data obtained from the strain gauges.

For the analysis of the results, the data obtained from the unloading tests were taken into account. At the beginning of the load phase, it was necessary to pull the springs slightly to put the cables in tension, as if they are not sufficiently pulled, they risk not winding well in the guide. In contrast, the unloading phase starts with a load applied to the gearbox and the springs are unloaded completely, thus resulting in a final load of zero. The initial tensioning of the load phases introduces variability into the load and testing, which is why the following considerations and results were made on the unloading phases.

Depending on the test performed, an FBG sensor or strain gauge can be in tension or compression. The deformations obtained for the sensor pairs arranged on the gearbox are illustrated next.

In order to make qualitative assessments of the behaviour of FBGs as prognostic sensors, the results relating to the individual test 4 are set out below. All other results for the other tests are set out in the appendix.

6.5.1 FBG Deformations

The wavelength variations on the FBGs and the strain gauges at position during test 4 (60 deg) are shown below.

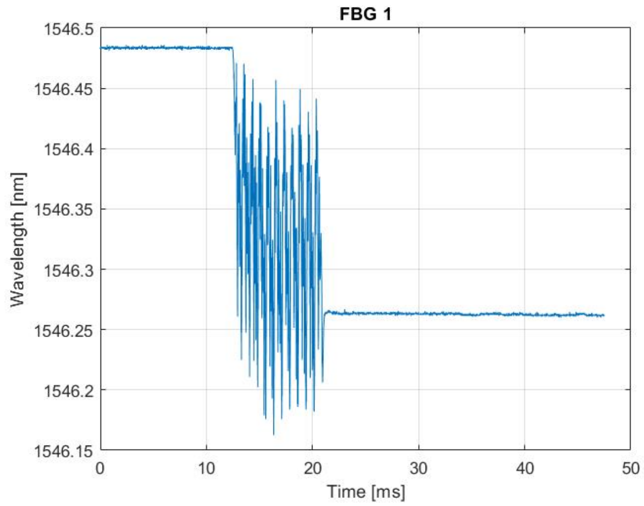

Figure 6.4. FBG1 (test 4)

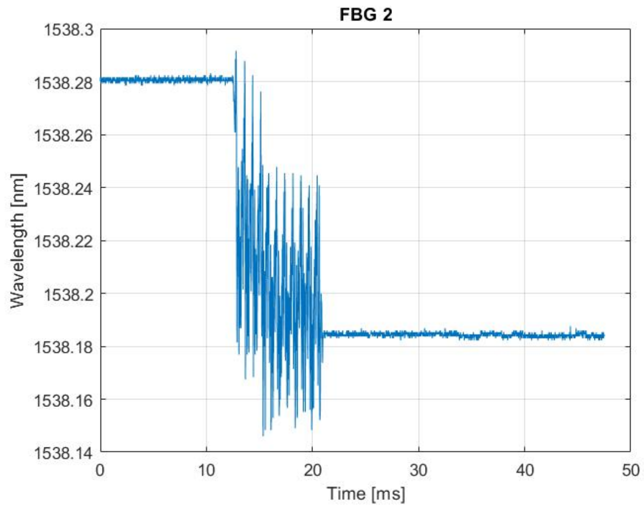

Figure 6.5. FBG2 (test 4)

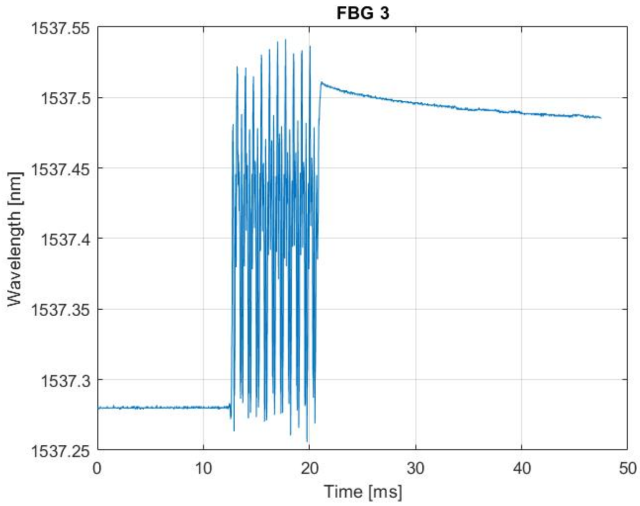

Figure 6.6. FBG3 (test 4)

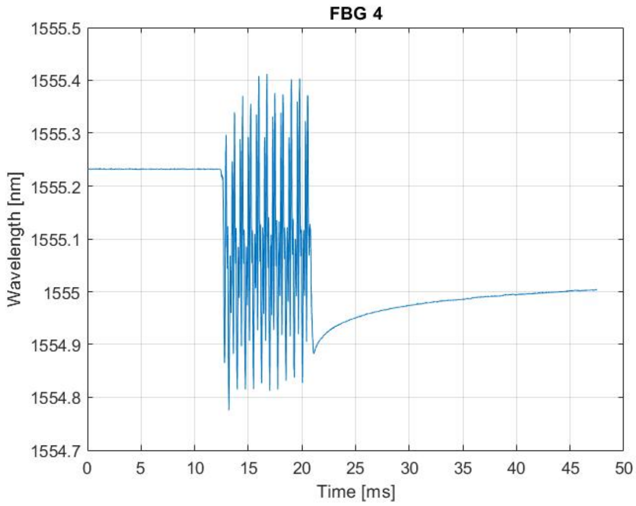

Figure 6.7. FBG4 (test 4)

In all 4 FBG sensors, 3 phases can be distinguished:

- **Initial steady state:** Torque is applied to the gearbox via the load module, so the FBGs measure a different wavelength than its rest wavelength, as the load induces a deformation of the gearbox structure and consequently a deformation on the FBGs. The wavelength is not constant but there are oscillations due to external disturbances, such as external vibrations.

- **Transient:**In this phase, the motor rotates and the servomechanism moves to reach the commanded end position. As can be seen, the fibers measure oscillations due to the vibrations induced by the rotation of the gearbox. In this phase, the peaks of the oscillations are periodic. This phenomenon is probably due to the fact that the motor is limited in speed, so when an instantaneous step command is given, the motor saturates in speed and the gearbox rotates at a constant speed. Consequently, the mechanical vibration due to the rotation of the gearbox and its gears is approximately periodic.

- **Final steady state:** The motor reaches the end position, then the load module applies no load on the gearbox, the FBGs stabilise on an initial resting wavelength. Although a condition of complete discharge is always reached in all the different tests, this final wavelength may differ from one test to another as the temperature of the room may change between the different tests, affecting the behaviour of the fiber.

In test 4, sensors 1,2,4 switch from a higher to a lower wavelength over time. In the first seconds of the test, FBGs 1,2,4 are tensioned and therefore have a higher wavelength than at rest but during unloading of the gearbox their wavelength decreases. In contrast, sensor 3 in the initial phase is compressed and has a shorter wavelength than in the final phase. (Figures 6.4, 6.5, 6.6, 6.7)

Note that, as can be seen in the figures 6.6 and 6.7, sensors 3 and 4 do not stabilise instantaneously at the final value after the transient, but show an approximately exponential trend. This behaviour is probably related to the plastic behaviour of the glue, which takes time to return to its resting condition.

What is observed is that the fibers were able to measure wavelength variations consistent with the test phases and that they also measured compression. Now the data collected by the strain gauges during the same test will be evaluated.

6.5.2 Strain Gauges Deformations

The deformations measured by the strain gauges during test 4 are shown below.

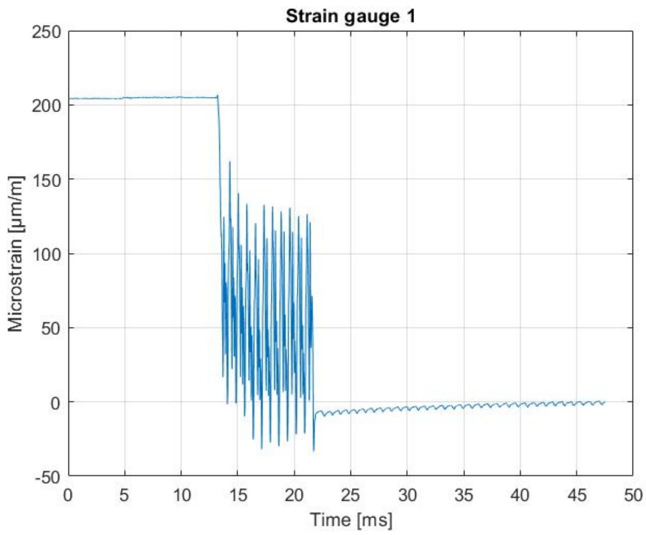

Figure 6.8. Strain Gauge 1 (test 4)

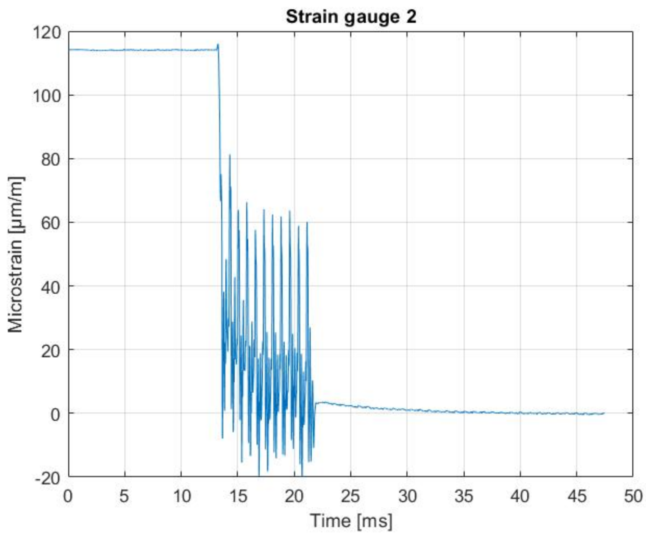

Figure 6.9. Strain Gauge 2 (test 4)

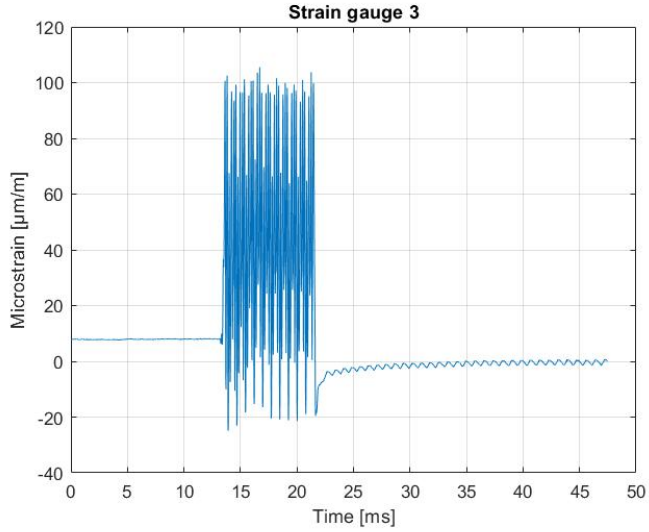

Figure 6.10. Strain Gauge 3 (test 4)

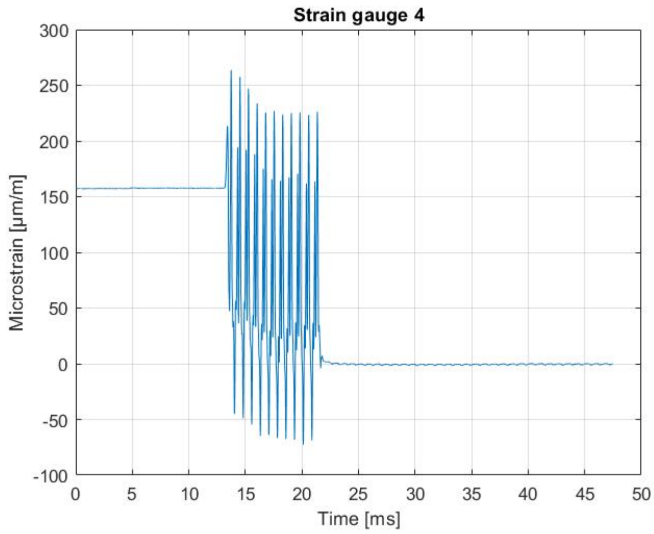

Figure 6.11. Strain Gauge 4 (test 4)

The strain gauges via the acquisition unit directly provide the measured strain in microstrain. Also in strain gauges as in FBGs, the 3 test phases can be distinguished: Initial steady state, transient and Finale steady state. In this test, a maximum strain of just over 200 microstrains was achieved on strain gauge 1. Consistent with what was observed in the fibers, strain gauges 1,2,4 are in a tensile state when the load is applied, then a transient phase with oscillations is observed and finally they settle to zero strain, as the load on the gearbox is zero at the end of the test. Strain Gauge 3 in this test, unlike the fibers, did not detect consistent deformation, but did detect transient vibrations; this may be due to the fact that Strain Gauge 3 is not on the same transverse axis as FBG3, so the strains on the two sensors are not of the same magnitude.

6.5.3 FBG and strain gauge comparison

Comparing the data from the various tests, it can be observed:

- **Sensors in position 1 and 4:** they always behave similarly, so when the fiber measures a compressive strain, the corresponding strain gauge also measures a compressive strain, same for tension.
- **Sensors in position 2 and 3:** There is not always a correspondence between what the strain gauge measures and what the FBG measures in the various tests. In some cases, the data are discordant or the strain gauges do not measure consistent deformations to be able to make qualitative assessments. This is due to the fact that strain gauges in these positions present installation problems: strain gauge 3 is not mounted on the same transverse axis as the FBG3, but slightly higher up and in a central position. Strain gauge 2, on the other hand, is not in a central position but is not on the same axis as the FBG2. These problems were due to the fact that the presence of the braking module on the side of sensors 2 and 3 considerably reduced the available operating space and made the installation of the sensors more complicated. However, it was decided to analyse the sensor data from sensors 2 and 3 in order to assess how inaccurate installation could affect the accuracy of the results.

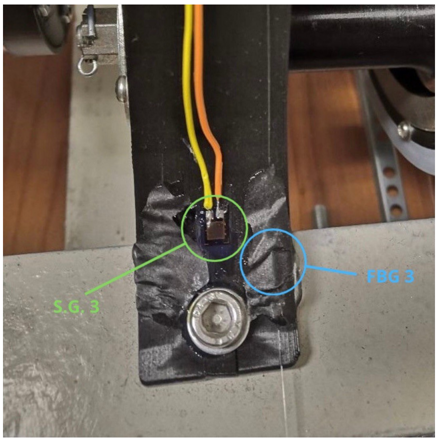

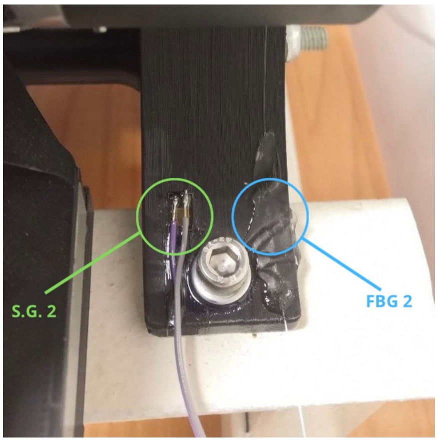

Figure 6.12. FBG and Strain gauges in positions 2 and 3

6.5.4 FBG-Strain Gauges synchronisation

The acquisition systems of FBGs and strain gauges are separate and it is not possible to synchronise them via hardware, so during the tests, the acquisitions have different time durations and a time delay, as the acquisition of the interrogator in all tests starts after that of the strain gauges. In order to be able to compare the data, it was necessary to synchronise the data in post-processing. For this purpose, Matlab software was developed which analyses the FBG and strain gauge signals and synchronises them. Specifically, the software isolates peaks due to load application and uses these references to synchronise the data. Transients in both strain gauges and fibers are very noisy, so for synchronisation the two signals were filtered using the moving average.

The graphs obtained from the synchronisation are shown below. Note that the graphs have two y-axes, one relating to the microstrains and thus the strain gauges, and the other relating to the wavelength in nm and thus the fibers. The two signals are not perfectly superimposed because they refer to two different physical quantities, however, these graphs are very useful for comparing the responses of the two sensors at steady state and in transient conditions and checking if there is a match.

In the Figure 6.13 the blue curve should be read on the blue axis in microstrain, conversely the orange curve represents the wavelength variation of FBG1 and its values should be read on the orange axis.

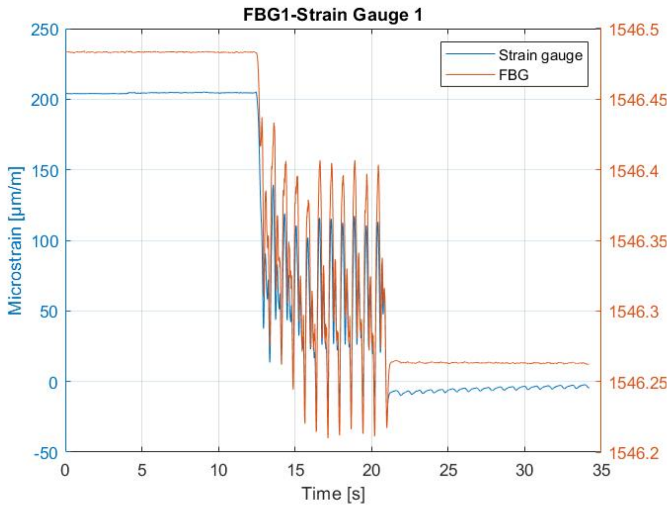

Figure 6.13. Synchronisation FBG 1 - Strain Gauge 1

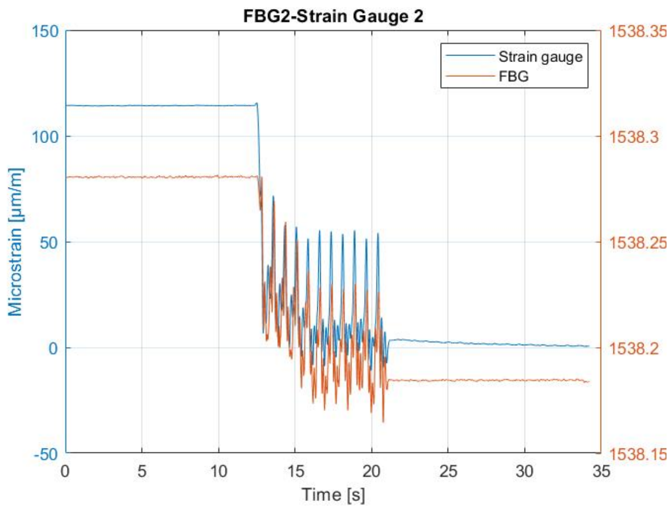

Figure 6.14. Synchronisation FBG 2 - Strain Gauge 2

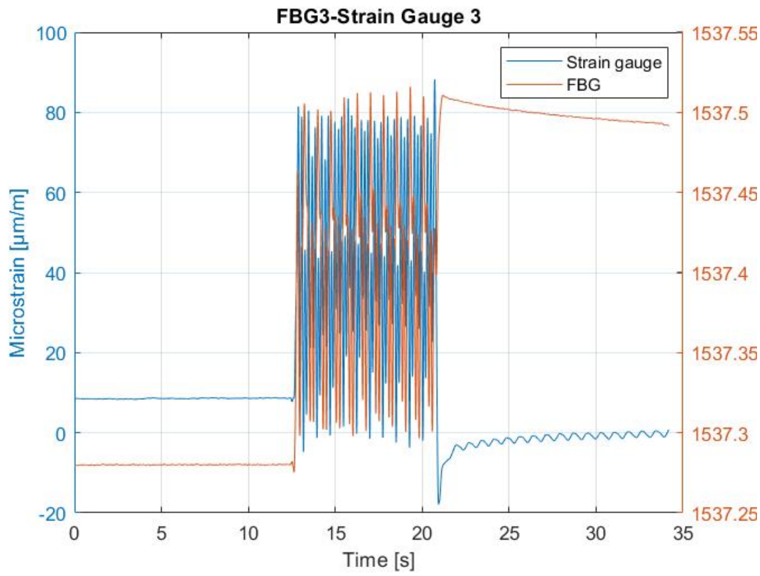

Figure 6.15. Synchronisation FBG 3 - Strain Gauge 3

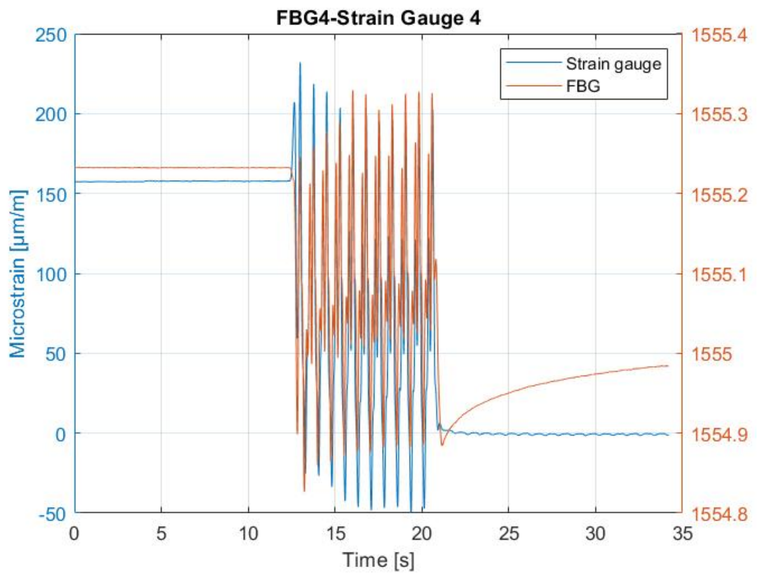

Figure 6.16. Synchronisation FBG 4 - Strain Gauge 4

On sensors 1,2,4, (Figures 6.13, 6.14, 6.16) it can be seen that the FBG and strain gauge trend is the same and that both respond in the same way to the applied load. On sensor 3 (Figure 6.15), on the other hand, it can be seen that the strain gauge does not measure any substantial deformations and, on the contrary, the fiber measures deformations and has the opposite trend. Furthermore, in sensor 4 the FBG has a slight exponential trend before reaching the resting wavelength, due to the plastic behaviour of the glue.

Synchronising the signals also allows the transient phase to be analysed, in order to qualitatively assess the behaviour of FBGs and strain gauges. Below are zooms on the transient phase, in which the gearbox is rotating to reach the commanded position and unloading. The transient phases of FBG 1 and strain gauge 1 are shown below (Figures 6.17, 6.18).

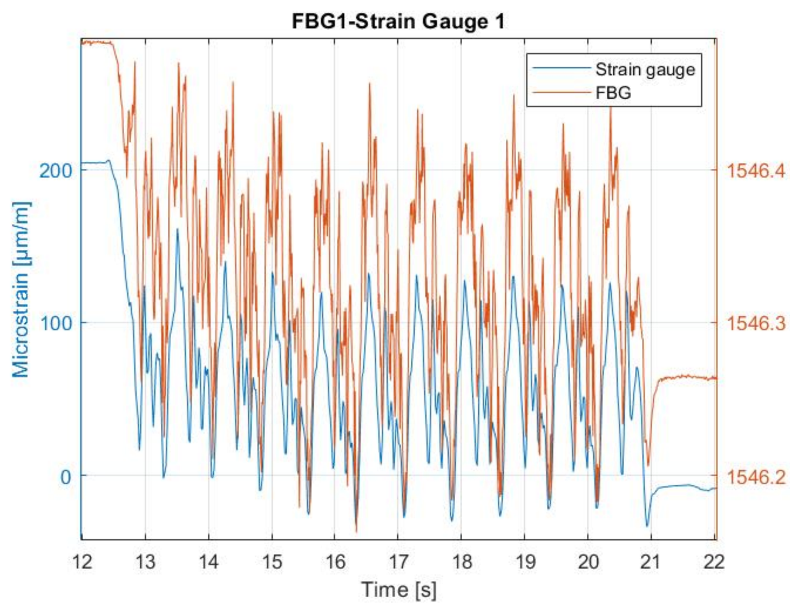

Figure 6.17. Not-Filtered Dynamic FBG 1 - Strain Gauge 1

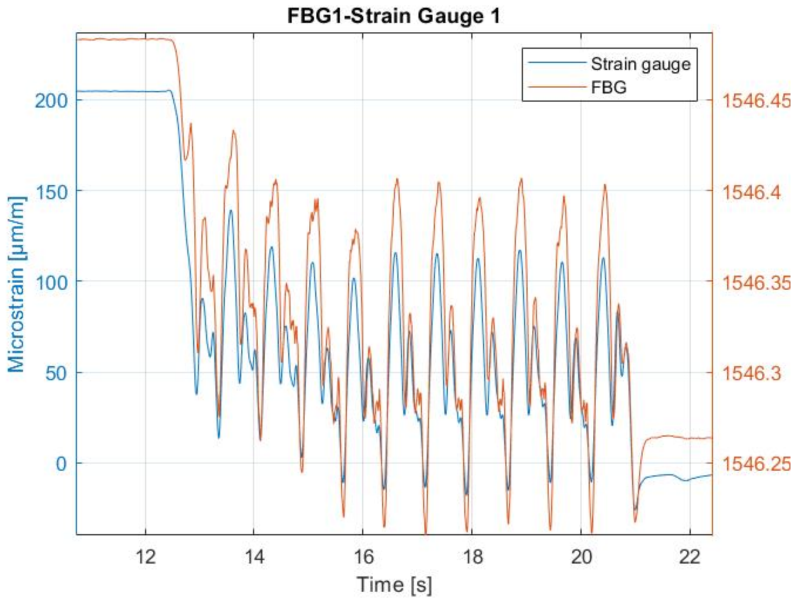

Figure 6.18. Filtered Dynamic FBG 1 - Strain Gauge 1

In the figure, the signals are superimposed unfiltered and filtered with moving average. Both strain gauges and FBGs have the same number of peaks and the same trend, demonstrating that both sensors detect the vibrations induced on the structure by the movement of the gearbox itself. Obviously, the graphs are not superimposed, as they refer to different physical quantities. In the following chapters, we will proceed with the calibration of the FBGs and thus obtain an estimate of the deformations in microstrain from the FBGs. It will then be possible to superimpose the graphs on the same scale and assess the accuracy of the FBGs in measuring deformations.

6.5.5 FBG Validation: K-calculation

The next step is the validation of FBGs as sensors for measuring mechanical strain. During the tests, the interrogator sends a laser signal into the optical fiber and reveals wavelength changes when the FBGs are subjected to a deformation. In order to use FBGs as strain sensors, it is necessary to correlate this wavelength variation to a deformation measured in microstrain . Data from strain gauges are used for this purpose.

Specifically, In the literature[6] is reported this equation that correlates the relative wavelength variation with the strain measured in microstrain:

$$\frac{\Delta\lambda_b}{\lambda_b} = K\epsilon \tag{6.1}$$

In the previous equation:

- $\Delta\lambda_b/\lambda_b$ is the relative change of the Bragg wavelength, this data is obtained from interrogator.
- ϵ is the mechanical strain, measured in microstrain by the strain gauge acquisition unit.
- K is a factor that represent the strain sensivity of FBGs.

For each FBG, data from all tests were collected and graphed, after which the regression line was calculated and K was estimated. The validation was carried out on the sensors installed in position 1 and 4 because they had better installation conditions, as seen in the previous paragraphs.

On the same FBG different deformations were obtained during different tests, because the load conditions change from test to test. To validate the FBGs, it was verified whether there is a linear correlation between strain measured by the strain gauge and wavelength variation, and the K-factor was calculated. Specifically for each sensor, the FBG and strain gauge data were plotted on a graph (ϵ, $\Delta\lambda_b/\lambda_b$).

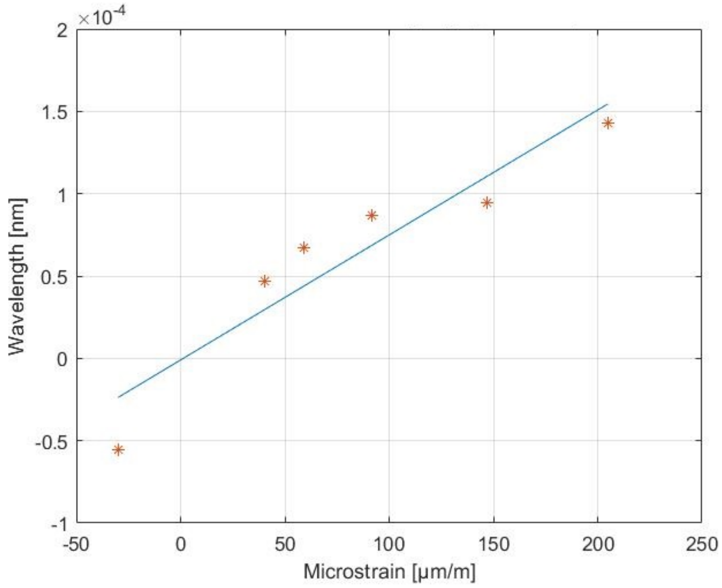

Figure 6.19. Relation FBG-Strain gauge (Sensor 1)

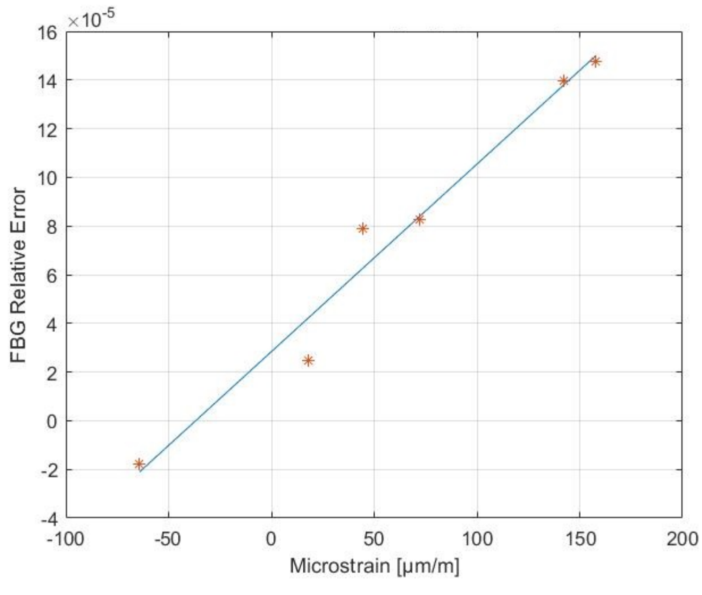

Figure 6.20. Relation FBG-Strain gauge (Sensor 4)

In Figures 6.19 and 6.20 the regression line that best represents the results obtained was plotted in blue. Each point represents data from a single test and on a single sensor (FBG and strain gauge). Strains within a range of just over 200 microstrains were obtained on both sensor 1 and sensor 4. On sensors 2 and 3, on the other hand, much smaller deformations in modulus were obtained and thus not functional for a calibration of the FBGs. The angular coefficient of the blue line represents the K-factor used to calibrate FBG1 and FBG4. It was obtained:

K (Fbg 1)	**0.77**
K (Fbg 4)	**0.78**

Table 6.3. K factors on Fbg 1 and Fbg 4

The results obtained are perfectly in line with theory, in fact a theoretical FBG gauge factor **K=0.78** is reported in the literature[6][5] . This shows that in spite of all the experimental factors that may influence the behaviour of FBGs, a result was obtained that corresponds to what is expected in the literature and thus allows fibers to be validated as sensors for mechanical deformation. As can be seen from the graphs, the points are not perfectly superimposed on the regression line. The presence of this experimental error may depend on several factors:

1. The physical characteristics of the material or glue can influence the optical characteristics of the FBG, changing the fiber refractive index.

2. The FBG sensivity is dependent on installation technique.

3. The coefficient K varies according to the type of FBG and its fabrication technique.

4. Temperature changes induce an additional wavelength variation on the FBG, a change of 1°C corresponds to approximately 8 microstrains of additional deformation[5]. There are no temperature sensors in these tests, so the temperature changes between tests, inducing changes in the behaviour of the fiber.

5. For practical reasons, the strain gauge and FBG are not mounted in the exact same place and therefore, as the structure is not isoptrophic, the actual

deformations may be slightly different.

Having calculated the K for the two FBG sensors, it is possible to use the K to transform the wavelength change measurement into the estimated strain. In this way, the strain measured by the FBGs can be traced from the data provided by the interrogator. Specifically, it results that:

$$\epsilon_{FBG} = \frac{\frac{\Delta\lambda_b}{\lambda_b}}{K} \tag{6.2}$$

The deformations of the FBGs were calculated using the equation 6.2 and were compared with those measured by the strain gauges. As can be seen in the figures 6.21 and 6.22, the graphs have the same trend, however, in the first part of the graph on the left, the curves are not perfectly superimposed. This is due to the fact that the estimated K is that of the regression line and the actual K is slightly different from test to test and is influenced by the factors outlined above. On sensor 1, a strain estimation error of approximately 15 microstrain was obtained. On sensor 4, a strain estimation error of about 30 microstrain was obtained. Furthermore, in the graph it can be seen that the strain estimated by the fiber has an exponential transient before reaching steady state, this may be due to the influence of the glue on the sensor.

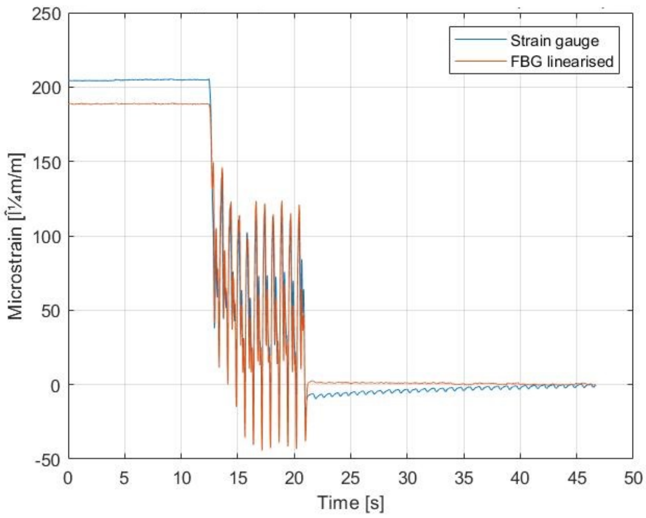

Figure 6.21. FBG estimated deformation - Strain gauge deformation (Sensor 1)

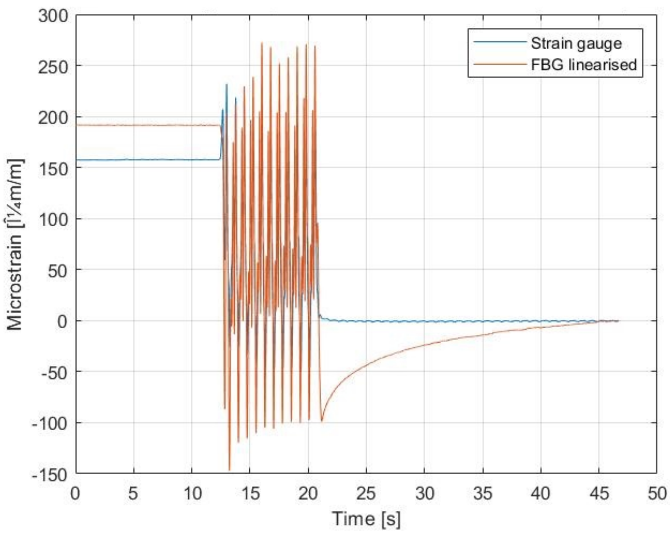

Figure 6.22. FBG estimated deformation - Strain gauge deformation (Sensor 4)

Through K, the deformations in the transient can also be reconstructed, as shown in figures 6.23,6.24.

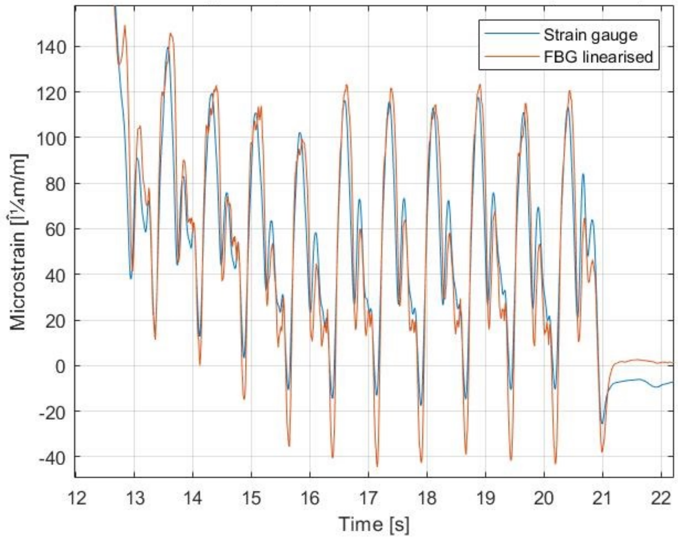

Figure 6.23. Dynamic of FBG 1 and strain Gauge 1

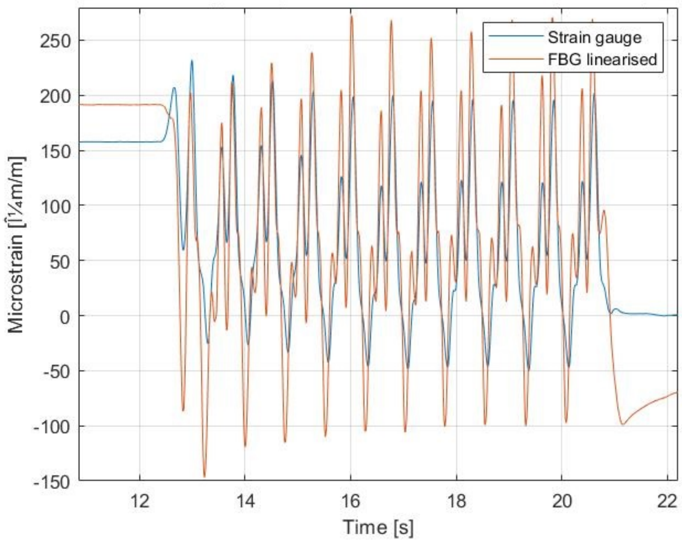

Figure 6.24. Dynamic of FBG 4 and strain Gauge 4

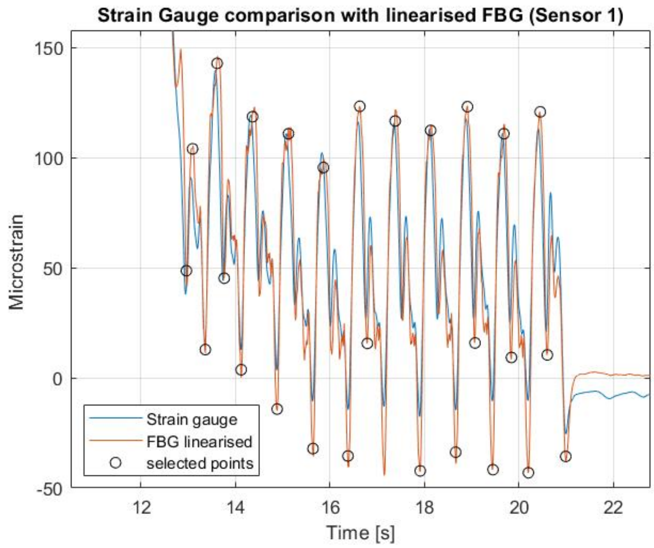

Figure 6.25. Selected points for discretization (Sensor 1)

From the graphs 6.25 it is visible that the transient pattern is the same for the FBG and the strain gauge, however, the FBG reaches higher peaks. This may be due to a higher sensitivity of the fiber to transient vibrations. The Pearson index was calculated to assess if there is a correlation between the transient measured by FBG1 and Straing Gauge 1. The transient was discretized into 27 different points, identifying the positive and negative peaks of the signal, and the index was calculated. For the same time instants of the selected points, the microstrain value measured by the FBG and the strain gauge was compared. In this way, 2 vectors of 27 elements were obtained and used to calculate the Pearson index. Deformations of FBG and Strain gauge, for the 27 points (time instants) were reported in Table 6.4.

Time [ms]	Strain Gauge [microstrain]	FBG [microstrain]
1296	38.69	48.62
1309	87.38	103.96
1336	13.74	12.84
1361	135.27	142.79
1376	47.30	45.24
1412	12.84	3.67
1436	115.00	118.56
1488	3.37	-14.17
1512	102.77	110.81
1564	-10.70	-32.13
1586	100.65	95.47
1638	-12.64	-35.47
1663	112.58	123.26
1679	33.21	15.63
1738	115.08	116.58
1791	-17.59	-42.24
1813	112.37	112.33
1866	-13.02	-33.76
1891	114.80	123.09
1907	32.96	15.82
1945	-10.52	-41.70
1968	109.22	110.81
1984	32.41	9.24
2020	-10.41	-43.10
2045	106.82	120.76
2060	24.98	10.38
2099	-24.54	-35.68

Table 6.4. Transient comparison FBG-Strain Gauge (sensor 1)

The Pearson correlation index ρ is used to assess a linear correspondence between two statistical variables: the index is always between -1 and +1. Depending on the value, the following correspondences occur:

- $\rho > 0$: positive correlation
- $\rho < 0$: negative correlation
- $\rho = 0$: no correlation

- $0<|\rho|<0.3$: low correlation
- $0.3<|\rho|<0.7$: moderate correlation
- $|\rho|>0.7$: high correlation

For 2 statistical variables X and Y the Pearson index is calculated as follows:

$$\rho_{xy} = \frac{\sigma_{xy}}{\sigma_x \sigma_y} \tag{6.3}$$

with the variables defined as follows:

- ρ_{xy}: Pearson index
- σ_{xy}: covariance between X and Y
- σ_x,σ_y: standard deviations

Comparing deformations measured by the strain gauges and the strains calculated from the FBG data (using the experimental K derived) resulted in a Pearson index of ρ=**0.9497**. A correlation coefficient of 0.9497 indicates that there is a strong positive correlation and thus proves that FBGs are also well suited to assessing time-varying deformations, in this case due to gearbox rotation. The distribution of points is shown in the figure6.26.

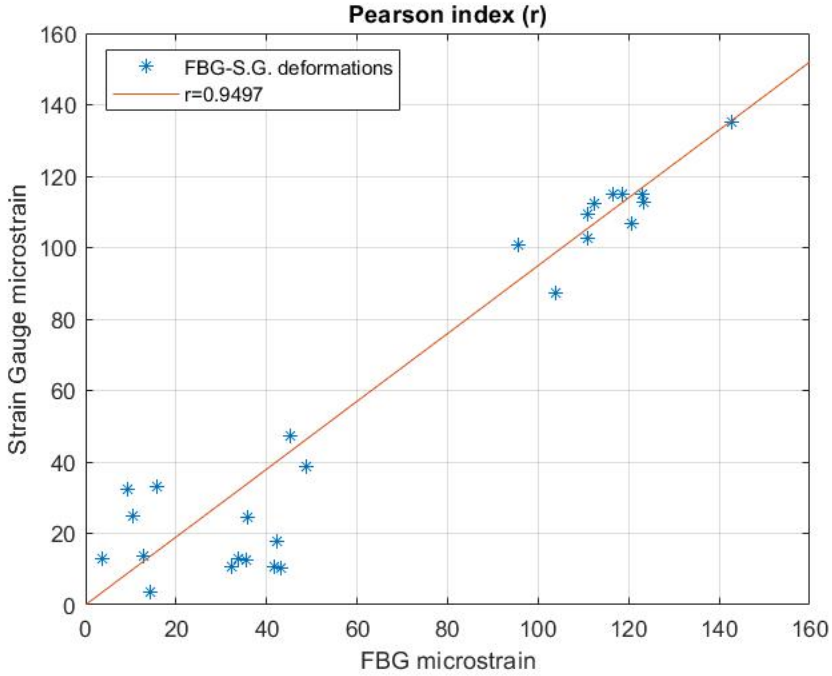

Figure 6.26. Pearson index: scatter diagram

As can be seen in the figure for smaller strains the points are far from the line, however as the strain value increases the points are distributed much closer to the line with an angular coefficient of 0.9497. This shows that as strain increases, the strain gauge and FBG data tend to coincide more closely and the accuracy of the FBG in measuring strain increases.

6.5.6 Oscillation analysis at steady state

In some of the tests performed when the motor reaches the commanded end position, a noticeable oscillation of the strains measured by the strain gauges and FBGs was observed. Analysing the data the control unit sends to the PC during the execution of the tests, a very similar oscillation was observed in the currents commanded by the control unit to the motor. This oscillation when the gearbox is unloaded indicates that the position measured by the encoder is not exactly the final position commanded.

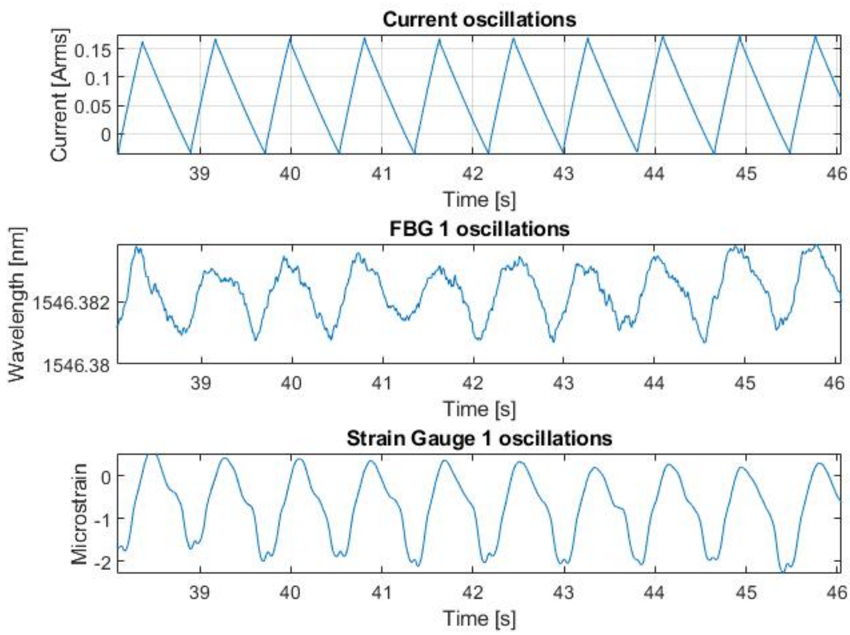

Figure 6.27. Oscillations in Current, FBG, Strain Gauge

This causes the control unit to command small currents to the motor to reach the desired position. However, probably due to internal backlash in the gearbox, the position measured by the encoder is never the commanded position, and consequently a cycle is set up that causes the currents to oscillate over time.

The oscillations detected by the FBGs seem to be attributable to these small commands, which the control unit sends out to compensate for gearbox backlash.

To check whether the oscillations are related to this motor behaviour, the FFTs of the strain gauge, FBG and driven current signals were calculated at the final instants of test 1.

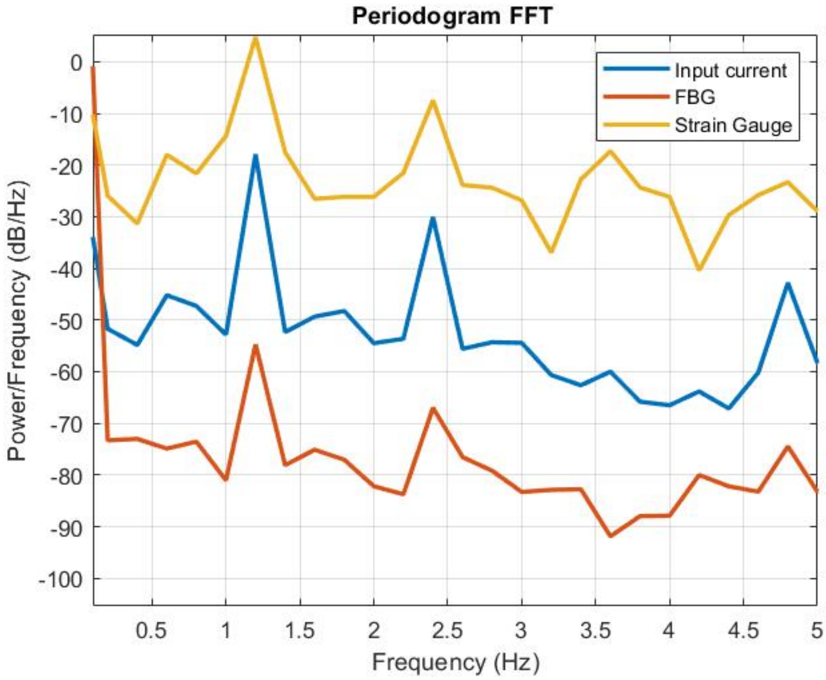

Figure 6.28. Periodogram

The frequency spectra of the 3 signals are very similar, in particular they show the same peaks at certain characteristic frequencies: 1.2 Hz and 2.4 Hz. This shows that FBGs are able to measure the small movements that the servomechanism makes to compensate for internal backlash. This is an important result as it demonstrates that FBGs can be used not only to assess that deformations do not exceed critical limits but also to be able to trace back servomechanism behaviour such as backlash compensation.

Chapter 7

Conclusions and future work

At the end of the thesis project, it was demonstrated that FBGs sensors are able to accurately measure the structural deformations of the Gearbox in both static and dynamic regimes. In fact, comparing the data with strain gauges, an excellent overlap of the signals was obtained even in transient conditions, with a good positive correlation (Pearson index=0.9497). It was observed that the accuracy of FBGs increases with increasing strain. It was possible to experimentally calculate a K-factor from the wavelength measurement directly to the deformation, and it was found that the K-factor is the same as reported in the literature. In addition, FBG sensors are able to detect oscillations perfectly attributable to the movement of the engine to compensate for internal gearbox backlash. This result is very interesting because it demonstrates that FBGs can also detect data that can be indirectly traced back to the wear of the servomechanism and its life cycle. This feature is very important for using FBG sensors for prognostic purposes. A future step that could be implemented is the introduction of temperature compensation, so being able to eliminate the influence of temperature on strain measurement.

Bibliography

[1] Caratteristiche meccaniche delle molle. Manutenzione aeronautica e PCM, Università degli studi di Enna.

[2] Strain gauge measurement – a tutorial. *National instruments*, Application Note 078, 1998.

[3] A. J. Forsyth A. A. AbdElhafez. A review of more-electric aircraft. *13th International Conference on AEROSPACE SCIENCES AVIATION TECHNOLOGY*, pages 1–13, 2009.

[4] Zhenghong Shi2 Yawen Wang3 Shangjun Ma1 Guan Qiao1, Geng Liu1 and Teik C Lim3. A review of electromechanical actuators for more/all electric aircraft systems. *Journal of Mechanical Engineering Science*, 232(22):4128–4151, 2017.

[5] Darmstadt Germany Manfred Keuzer, HBM. Strain measurement with fiber bragg grating sensors.

[6] A. Zoccoli. P. Boccaccio, R. Donà. Calibration of a fiber bragg grating as ultra-sensitive strain gauge. *Istituto Nazionale di Fisica Nucleare, LNL Annual Report*, pages 191–192.

[7] P Maggiore P C Berri, M D L Dalla Vedova and T Scolpito. Feasibility study of fbg-based sensors for prognostics in aerospace applications. *Journal of Physics: Conference Series 1249*, pages 1–8, 2019.